Subpixel Characterization of HIRS Spectral Radiances Using Cloud Properties from AVHRR

PAUL W. STATEN

Indiana University, Bloomington, Indiana

BRIAN H. KAHN AND MATHIAS M. SCHREIER

NASA Jet Propulsion Laboratory, California Institute of Technology, Pasadena, California

ANDREW K. HEIDINGER

NOAA/NESDIS/Center for Satellite Applications and Research, Madison, Wisconsin

(Manuscript received 15 September 2015, in final form 18 March 2016)

ABSTRACT

This paper describes a cloud type radiance record derived from NOAA polar-orbiting weather satellites using cloud properties retrieved from the Advanced Very High Resolution Radiometer (AVHRR) and spectral brightness temperatures (T_b) observed by the High Resolution Infrared Radiation Sounder (HIRS). The authors seek to produce a seamless, global-scale, long-term record of cloud type and T_b statistics intended to better characterize clouds from seasonal to decadal time scales. Herein, the methodology is described in which the cloud type statistics retrieved from AVHRR are interpolated onto each HIRS footprint using two cloud classification methods. This approach is tested over the northeast tropical and subtropical Pacific Ocean region, which contains a wide variety of cloud types during a significant ENSO variation from 2008 to 2009. It is shown that the T_b histograms sorted by cloud type are realistic for all HIRS channels. The magnitude of T_b biases among spatially coincident satellite intersections over the northeast Pacific is a function of cloud type and wavelength. While the sign of the bias can change, the magnitudes are generally small for *NOAA-18* and *NOAA-19*, and *NOAA-19* and *MetOp-A* intersections. The authors further show that the differences between calculated standard deviations of cloud-typed T_b well exceed intersatellite calibration uncertainties. The authors argue that consideration of higher-order statistical moments determined from spectral infrared observations may serve as a useful long-term measure of small-scale spatial changes, in particular cloud types over the HIRS–AVHRR observing record.

1. Introduction

A global observational dataset that is spectrally broad, spectrally resolved, and traceable to absolute standards is desirable for detecting and monitoring climate change (Anderson et al. 2004). There is a record of well-calibrated hyperspectral midinfrared and visible/near-infrared narrowband observations from the Atmospheric Infrared Sounder (AIRS), but it extends back only to the launch of EOS *Aqua* in 2002. Therefore, it is imperative to characterize the capabilities of past and present weather observing systems for the purpose of observing some key climate observables, such as narrowband radiances and the cloud types they are associated with, in order to build a useful climate record that has an increased probability of capturing atmospheric trends caused by anthropogenic climate change.

NOAA polar-orbiting satellites have been in orbit since the launch of *TIROS-N* in 1978, and currently a new generation of instruments (very similar to EOS *Aqua*) is available on board the *Suomi NPP* (formerly NPOESS Preparatory Project) satellite platform. Each of these operational satellite systems, up until the launch of *Suomi NPP*, carries the Advanced Very High Resolution Radiometer (AVHRR) and the High Resolution Infrared Radiation Sounder (HIRS). Although incremental changes have been made to both AVHRR and HIRS with successive launches, the overall configuration has

---

Corresponding author address: Paul W. Staten, Indiana University, 1001 E. 10th St., Bloomington, IN 47405-1405.
E-mail: pwstaten@indiana.edu

DOI: 10.1175/JTECH-D-15-0187.1

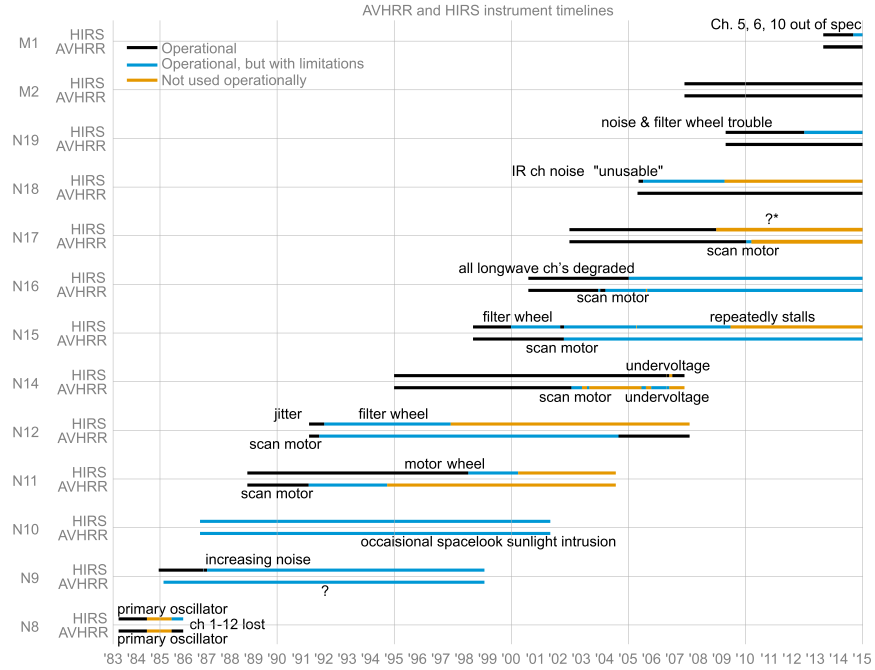

FIG. 1. Timeline of NOAA polar-orbiting satellite instrument status. For each satellite, the instrument status for HIRS (upper) and AVHRR (lower) is denoted by color, as shown in the legend. Reasons for changes in status are noted, where known. "Not operational" denotes data not being used operationally, and it does not necessarily imply that no data are available. One notable example of this is the HIRS/4 instrument aboard *N18*, which is still producing data, albeit with substantial noise. The asterisk (*) denotes that AVHRR aboard *N17* is still operational after January 2009, but we avoid data from this time period. The question mark (?) denotes status changes for which the cause is not known by the authors.

changed little (Fig. 1). In addition, the European Organisation for the Exploitation of Meteorological Satellites (EUMETSAT) recently launched two weather satellites, *MetOp-A* and *MetOp-B* (top rows in Fig. 1), each containing new and more capable instruments along with the legacy AVHRR and HIRS instruments. MetOp-C will also carry an AVHRR but not a HIRS. While the observational record has considerable uncertainty, a clear advantage of the combined AVHRR–HIRS record is that it spans over three decades and continues to lengthen. The International Satellite Cloud Climatology Project (ISCCP) (Rossow and Schiffer 1991) is commonly used to assess cloud changes over the last 35 years. However, while ISCCP has shown some skill in detecting latitudinal shifts in cloud fraction (Bender et al. 2011; Marchand 2013), there are limitations in this dataset that need to be corrected for with regard to cloud type trend detection (Norris and Evan 2015). Furthermore, the single infrared 11-μm channel that is made available is not capable of resolving spectral IR changes in clouds simultaneously within window and absorbing bands. These narrowband IR observations are available from the HIRS instruments but remain highly underutilized as a full spectrum for assessment of clouds, their adjacent thermodynamic environments, and covariances among the radiances between channels.

The intersatellite biases within the NOAA polar orbiter data record, due to both uncertainties in spectral response functions and orbital drift in the presence of a diurnal cycle, have hampered the construction of a rigorous and comprehensive dataset for all of the climate-related variables these instruments are capable of characterizing. While climate data records (CDRs) have been created using cloud properties from AVHRR (Foster and Heidinger 2013; Sun et al. 2015), the radiance CDRs derived from HIRS data have not been exploited for discerning spectral infrared features among different cloud types, which is potentially richer than that available from AVHRR alone. Furthermore, HIRS and AVHRR data have not been combined to investigate spectral IR cloud changes in the context of climate variability, let alone a changing climate. Previous research efforts such as Frey et al. (1996) used AVHRR to screen for clouds, and Baum et al. (1992, 1994) used selected HIRS channels to improve cloud type determination. But these studies, along with intercalibration studies such as Chen et al. (2013), often focus on a few channels at a time, precluding the investigation of relationships between cloud types and brightness temperatures T_b across the HIRS spectrum.

With the long-term goal of creating a climate-quality cloud type radiance record, the objectives of the present study are to prototype and test a scalable method for merging the visible and near-infrared cloud properties from AVHRR with the multispectral brightness temperature data from HIRS. Such a dataset facilitates multispectral cloud T_b trend detection in the face of instrument degradation and replacement. The preservation of higher moments enables the detection of process- and phenomenon-specific changes (e.g., changes in convection during El Niño, as we highlight in the present study). Future simulation of AVHRR and HIRS observations from general circulation models (GCMs) will allow both the benchmarking of the GCMs themselves (Turner and Tett 2014) and multispectral optimal fingerprinting of climate change.

As a first step toward creating a combined climate-quality dataset, we perform the following tasks for the present study.

1) We characterize HIRS spectral infrared T_b at a pixel-scale level by determining the cloud type(s) that are present within each HIRS pixel. We interpolate the AVHRR radiances and their derived cloud types onto HIRS pixels by testing several representations of the HIRS point spread function (PSF). After the interpolation is optimized and tested, we project the AVHRR-derived cloud type data based on Clouds from AVHRR Extended (CLAVR-x) cloud property retrievals onto HIRS pixels.
2) We spatially and temporally grid the cloud-typed HIRS spectral T_b. The gridding methodology is computationally efficient so that it can be performed for large sets of satellite data. Each full histogram contains the relevant statistical information of the cloud-typed T_b for that grid cell, which includes means, standard deviations, and additional higher-order moments.
3) We test our PSF interpolation and gridding methodology in the northeast Pacific Ocean region to determine whether the current state of the HIRS and AVHRR data is sufficient for discerning local, cloud type–specific changes in HIRS T_b statistics from ENSO variability apart from impacts due to HIRS spectral response function shifts, spatial resolution, diurnal sampling, and seasonal variability. We assess these impacts using selected satellite intersects in the northeast Pacific Ocean region during the years 2008 and 2009, in which a moderate strength shift in ENSO is observed.

This paper is arranged as follows. We first describe the NOAA polar orbiters and instruments, and the CLAVR-x cloud product retrieval methodology, in section 2. We then describe the interpolation procedure in section 3, the construction of the gridded datasets in section 4, and present results from the northeast Pacific Ocean case study in section 5. We summarize, conclude, and describe future directions of this work in section 6.

2. Data

The polar orbiter data are obtained from the NOAA Comprehensive Large Array-Data Stewardship System (CLASS) archive (http://www.class.ngdc.noaa.gov/). We focus on a subset of data from several recent NOAA platforms (*NOAA-16* onward, referred to in this study as *N16*, *N17*, and so on) and two EUMETSAT platforms (*MetOp-A*, referred to as *M2*; and *MetOp-B*, referred to as *M1*). All of these aforementioned satellites are in a polar low-Earth orbit, with the ascending (northward) track typically during the daytime and the descending (southward) track at nighttime 12 h later. While the EUMETSAT orbiters are in a controlled orbit, the ascending and descending equatorial crossing times (ECTs) for the older NOAA satellites drift over time (Fig. 2).

Traditionally, simultaneous nadir overpasses (SNOs), or some less stringent matching criteria, are used to compare data from multiple satellites. The most commonly used approach is to examine SNOs in high latitudes, which occur regularly for most pairs of polar-orbiting satellites. The approach we use in this study is to examine intersections at lower latitudes than SNOs either 1) when ascending ECTs for two satellites overlap and they cross the equator going the same direction at the same LST, or 2) when ascending and descending ECTs for two satellites overlap and they cross the equator going the opposite directions at the same LST. *N18* and *N19* experience an ascending ECT overlap in late 2009, and *N16* and *M1* experience an ascending–descending ECT overlap in early 2014 (see the solid red circles in Fig. 2). There is an additional ascending ECT overlap between *N17* and *M2* in mid-2009, but problems with *N17* after January 2009 prevent us from making a useful comparison during this overlap (see the dotted red circle in Fig. 2).

We analyze infrared T_b from HIRS, version 3 (on board older satellites, including *N16* and *N17*), and HIRS, version 4 (on board *N18*, *N19*, *M2*, and *M1*). These instruments operate via the use of a telescope, an

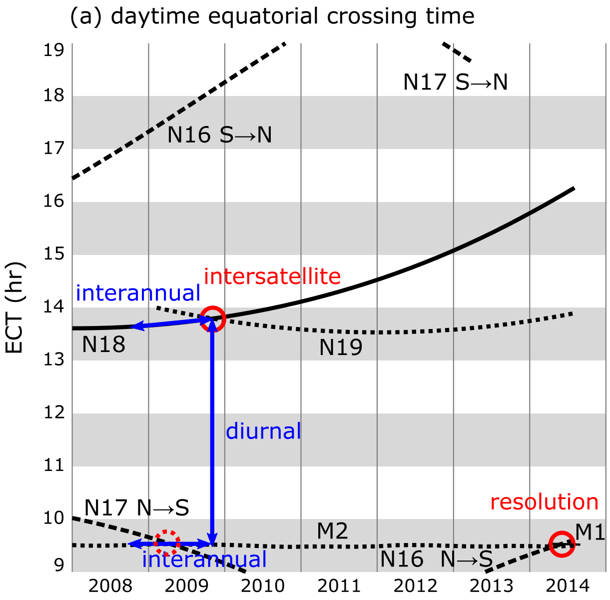

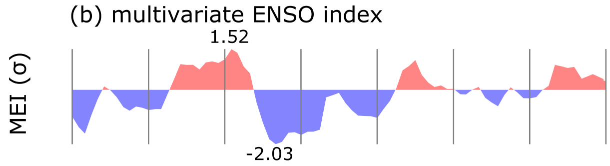

FIG. 2. (a) Daytime (either ascending or descending) ECTs for the polar-orbiting satellites examined in this study. Dashed lines represent platforms bearing the ~20-km HIRS/3 instrument, while solid and dotted lines represent platforms bearing the ~10-km HIRS/4 instrument. Red solid circles denote ECT overlaps analyzed in our northeast Pacific case study, and blue solid annotations illustrate comparisons depicted in later sections, as labeled. The ECT overlap between *N17* and *M2* during 2009 is also circled in dotted red, but no cloud type information is available for *N17* during this time period, as discussed in the text. During 2010, the ascending *N16* and descending *NOAA-17* ECTs drift outside the hours plotted, and the respective descending and ascending ECTs drift into the hours plotted a few years later. (b) The multivariate ENSO index (in standard deviations) taken from NOAA's Earth System Research Laboratory during the same time period, with blue shading denoting La Niña conditions and red shading denoting El Niño conditions.

elliptical scan mirror, and a rapidly rotating filter wheel containing 20 filters (Robel 2009). Both versions include one visible channel (0.63 μm), seven shortwave IR channels (3.7–4.6 μm), and 12 mid-IR channels (6.7–15 μm). Many of these channels are chosen to sample various layers of the atmosphere, and we refer the reader to Fig. 2 in Li et al. (2000) for the vertical weighting functions of HIRS/3 channels for the standard atmosphere. HIRS/4 has a resolution of about 10 km in the horizontal, while HIRS/3 has a resolution closer to 20 km; we derive a more precise estimate in section 3.

HIRS calibration fits measured scene counts to a quadratic calibration curve, which is based on regular views of outer space and internal blackbody targets. Under nominal operation, for most channels, HIRS calibration errors can be kept to within about 0.5 K (Cao et al. 2007). However, intersatellite calibration must account for not only the T_b calibration errors for a given satellite, but also for changes in the observed spectra from one satellite to the next. Postlaunch spectral response function changes can result in mean intersatellite biases as much as 4% from one satellite to the next for mid-IR channels (Chen et al. 2013). Shi et al. (2008) model these T_b biases as scene dependent, while Chen et al. (2013) apply a multichannel linear model to remove intersatellite biases in three mid-IR channels, constraining biases to within 1% for those channels.

For HIRS cloud type characterization, the visible and infrared imager data from AVHRR, version 3, on board all of the satellites, are exploited in this study. AVHRR samples up to three visible channels (0.5, 0.8, and 1.6 μm) and up to three IR channels (3.6, 11, and 12.5 μm), with a resolution of 1.09 km. However, the 3.6- and 1.6-μm bands cannot sample simultaneously. While the new MetOp orbiters are able to obtain global maps at this spatial resolution, limited data storage and transmission bandwidth limitations on the legacy NOAA systems required that the data be subsampled and degraded at a lower resolution. These Global Area Coverage (GAC) data are produced by retaining every third scan line along track, and averaging four of every five pixels across track, resulting in a nominally 4-km dataset (Frey et al. 1996). It is these 4-km pixels that we use in this study.

The cloud types are obtained from the CLAVR-x postprocessing routine (Heidinger et al. 2002, 2004; Thomas et al. 2004; Heidinger et al. 2014) applied to the AVHRR data. This is the operational version of the cloud processing routine used to produce the PATMOS-x CDRs, the only differences being that PATMOS-x makes use of a different reanalysis package and that it includes additional ancillary data in order to meet the specific requirements of a NOAA CDR. Our implementation of CLAVR-x makes use of auxiliary data from the National Centers for Environmental Prediction–National Center for Atmospheric Research Reanalysis 1 (NNR) product (Kalnay et al. 1996). These data are necessary as the cloud property retrievals are physically based. We also use these NNR fields directly in the case study analysis in section 5, interpolating in time between NNR time steps to the satellite observation time.

CLAVR-x uses a naive Bayesian methodology to detect clouds (Heidinger et al. 2012). Cloud phase and type are calculated using a series of thresholds described in Pavolonis et al. (2005) and Pavolonis and Heidinger

(2004). Other cloud properties are derived through split-window observations (Heidinger and Pavolonis 2009) and optimal estimation (Walther and Heidinger 2012). For a summary description of the cloud property retrieval methodology, we refer the reader to Heidinger et al. (2014).

We make use of two sets of cloud type information. The first set of cloud types (CLAVR-x cloud types) is directly output from the CLAVR-x routine using a split-window method that utilizes IR channels to produce a consistent day and night cloud retrieval. These cloud types are partitioned into *clear*, *probably clear*, *near surface*, *water*, *supercooled water*, *overlapping*, *opaque ice*, *cirrus*, and *overshooting* scene types. About 43% of the HIRS/4 pixels are uniquely associated with a single cloud/scene type, while the other 57% are composed of mixtures (see section 4). The second set (ISCCP cloud types) involves applying ISCCP binning thresholds on the cloud-top pressure and cloud optical depth output from CLAVR-x. These cloud types are partitioned into *clear*, *cumulus*, *stratocumulus*, *stratus*, *altocumulus*, *altostratus*, *nimbostratus*, *cirrus*, *cirrostratus*, and *deep convection*. About 51% of the HIRS/4 pixels are uniquely associated with a single cloud/scene type, while the other 49% are composed of mixtures. As these two cloud type approaches have their greatest strength using visible and IR channels, we herein focus on daytime cloud statistics only in the remainder of this work. This also helps to avoid any issues with differences in cloud-typing due to the switch from the AVHRR 1.6-μm channel to the 3.6-μm channel that often takes place during the night.

3. Interpolation of AVHRR pixels to the HIRS footprints

Our first objective is to characterize the cloudiness of HIRS/3 and HIRS/4 footprints from CLAVR-x data. A determination of which clouds are sensed by each HIRS observation is necessary. To this end, the HIRS PSF is reconstructed (see the schematic in Fig. 4). The PSF is an optimized weighting function applied to the higher-resolution imager data, to approximate what the HIRS instrument would observe if it included channels spectrally identical to those on AVHRR. The data necessary to optimize the reconstruction comes from HIRS channel 8 and AVHRR channel 4, with central wavelengths near 11 μm. The PSF is optimized by minimizing the root-mean-square (RMS) difference between the HIRS window channel (channel 8) and the interpolated AVHRR window channel (channel 4) radiances. The same window channels have been applied for the purpose of matching HIRS and AVHRR data by Baum et al. (1992) and others. The window channels allow straightforward optimization of the PSF, which can then be applied to CLAVR-x output to estimate the fraction of a HIRS footprint covered by a particular cloud type. Similar techniques have been previously used by Schreier et al. (2010) to combine narrowband imagery from the Moderate Resolution Imaging Spectroradiometer (MODIS) with hyperspectral infrared radiances from AIRS on board the *Aqua* satellite.

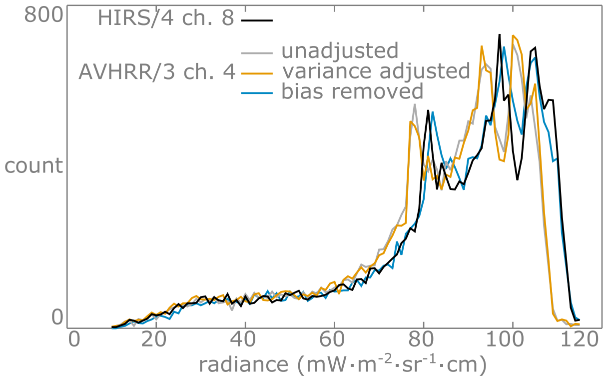

FIG. 3. Histograms of HIRS/4 (black) and AVHRR/3 (colors) radiances from *N19* (milliwatts per square meter per steradian per inverse centimeter) during 15 September–15 December (SOND) 2009 over the northeast Pacific. The gray, yellow, and teal curves represent the changing histograms of interpolated AVHRR/3 data after successive stages of adjustment.

Our procedure for optimizing the PSF is described below. Note that steps 1–5 constitute a series of checks to remove any suspect data. Steps 6 and 7 amount to the application of a linear least squares regression between interpolated AVHRR radiances and HIRS radiance statistics. These steps are repeated for each candidate PSF, and the PSF that produces the smallest RMS differences between the HIRS and the bias- and variance-corrected AVHRR window channel data for a given satellite is used for the remainder of the study.

1) Remove calibration scan lines and blank scan lines from AVHRR data.
2) Consider only sequences of AVHRR data with 100 nearly contiguous rows (with a gap in the row time of less than 3.6 s).
3) Apply each of the selected candidate PSFs, as well as a nearest-neighbor averaging approach, to interpolate AVHRR data onto HIRS footprints.
4) Throw out interpolated AVHRR rows that contain footprints with the 0.1% most extreme differences from the corresponding HIRS window channel data. This amounts to roughly 5% of AVHRR rows.
5) Throw out interpolated AVHRR rows with the 5% most extreme row-median differences in the window channel (the resulting distribution of radiances is illustrated in Fig. 3, gray curve).

6) Scale the departures of the interpolated AVHRR window channel data from the mean such that the variance of the interpolated AVHRR and the HIRS windows channel datasets match (Fig. 3, yellow curve).
7) Remove the median interpolated AVHRR-minus-HIRS window channel bias from the remaining interpolated AVHRR data (Fig. 3, blue curve).
8) Calculate the RMS differences between the interpolated AVHRR data, and the corresponding HIRS footprints (Fig. 3, black curve).

The candidate PSFs (and nearest-neighbor approach) examined in step 3 are described below and are depicted in Fig. 4. Aside from the nearest-neighbor approach, we mainly test PSFs with radii between 0 and 40 km.

Nearest neighbor (Fig. 4a): The nearest-neighbor approach assigns the value of the AVHRR 4-km pixel with the nearest HIRS footprint center.

Top-hat PSF (Fig. 4b): Circular top-hat PSFs with radii ranging from 0.4 to 40 km are tested. In the practical limit of a 2-km radius, this amounts to a nearest-neighbor approach.

Trapezoidal PSF (Fig. 4c): To account for aliasing along the outside of the top-hat PSF edge, we apply a hybrid trapezoidal PSF that amounts to a top-hat PSF with tapered edges, or a cropped conical PSF. The trapezoidal PSFs are tested with inner radii ranging from 0.4 to 40 km. For each inner radius, the PSFs with the distance between inner and outer radii ranging from 0.4 to 40 km are tested. In the limit of 2 km, this again amounts to a nearest-neighbor approach. In the limit of an inner radius of 0 km, this amounts to a conical PSF.

Conical PSF (Fig. 4d): Conical PSFs with radii ranging from 0.4 to 40 km are tested. PSFs with radii smaller than about 2 km amount to a nearest-neighbor approach.

Gaussian PSF (Fig. 4e): Gaussian PSFs defined by standard deviations ranging from 0.4 to 40 km are tested.

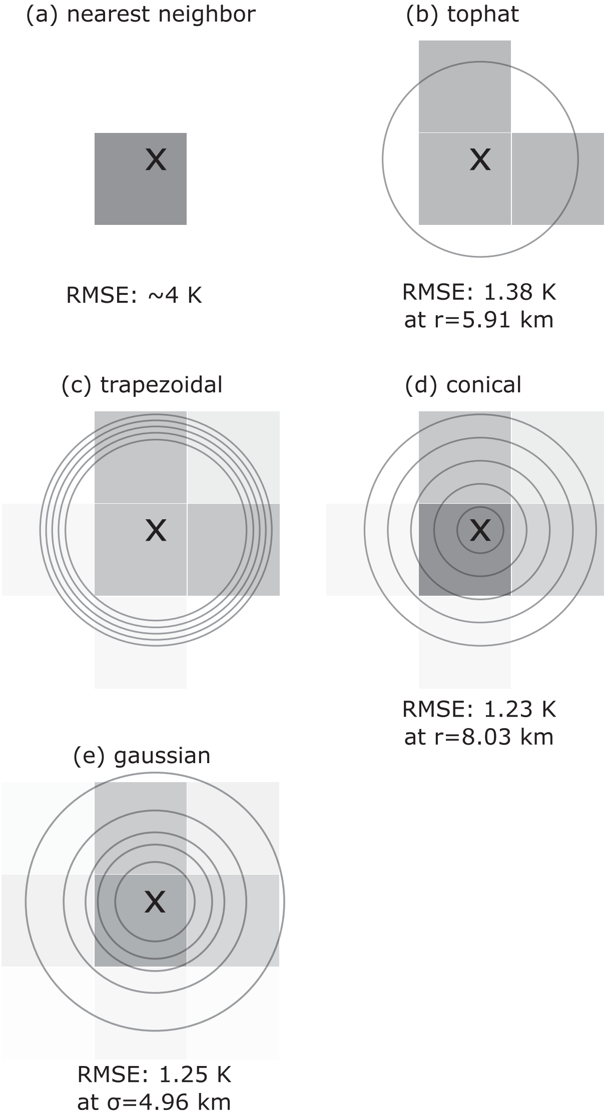

FIG. 4. Schematics of the PSFs, including the nearest-neighbor approach, as labeled. The center of the HIRS footprint is shown with an "x." The relative weighting function for each type of PSF is shown in contours. The relative weights received by the neighboring AVHRR pixels are represented with shading, with darker colors representing larger weights. RMSE between HIRS channel 8 and interpolated AVHRR channel 4 aboard *N18* are shown for the best of each footprint. These RMSE values are taken from data over our study region on 16 Nov 2009. The RMSE value is not shown for the trapezoidal PSF, because the best trapezoidal averaging function had an inner radius of zero, i.e., it was the conical PSF.

Corrected window channel RMS differences for the nearest-neighbor approach (Fig. 4a) were between 4 and 4.7 K for HIRS/3 instruments on board NOAA satellites, and 2.7 K for *M2* in our test dataset. These values are 3–4 times larger than the best RMS values for the other approaches, as the nearest-neighbor approach fails to incorporate information from a substantial portion of the HIRS footprint. The top-hat PSF (Fig. 4b) generally underperforms compared to the other PSFs, possibly due to aliasing on the edges of the PSF. The AVHRR 4-km pixels whose centers lie outside the top hat are ignored, even if the footprints overlap. The best trapezoidal PSFs (Fig. 4c) were those nearest to the conical limit, and the conical PSF (Fig. 4d) unsurprisingly outperforms the top hat and trapezoidal PSFs. The best Gaussian PSFs (Fig. 4e) perform nearly as well as conical PSFs when the difference between

TABLE 1. Optimal conical PSF radius and RMS differences in radiance between AVHRR channel 4 and HIRS channel 8 after bias removal and variance adjustment for conical PSF for November 2009 (or March 2014 in the case of *M1*). Smooth RMS represents the component of the RMSE that remains after Gaussian smoothing, and fine RMS represents the component of the RMSE remaining after subtracting the smoothed field. See Fig. 6

Platform	Radius (km)	RMS	Smooth RMS	Fine RMS
N16	17.72	1.57	0.53	1.39
N17	16.54	1.58	0.61	1.35
N18	8.03	1.4	0.57	1.23
N19	8.74	1.5	0.6	1.32
M2	7.56	1.01	0.46	0.84
M1	7.80	1.08	0.42	0.94

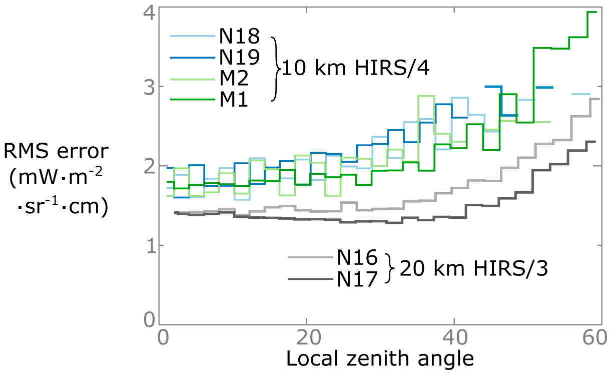

FIG. 5. Along-track RMS radiance differences between interpolated, shifted, and scaled AVHRR channel 4 radiances and HIRS channel 8 radiances, as a function of the absolute zenith angle on 16 Nov 2009 (or March 2014 in the case of *M1*).

their cross-sectional profiles is minimized, although the conical PSF is numerically faster. The radii, which produce the lowest corrected RMS values, are about 17 and 8 km for HIRS/3 and HIRS/4, respectively, which have widths at half-maximum weight near their reported footprint diameters of 20 and 10 km, respectively (see Table 1).

The conical PSF is applied to AVHRR pixels for all valid HIRS footprints, including both nadir and off-nadir viewing angles. While RMS errors (RMSE) between the HIRS radiances and the interpolated AVHRR radiances increase with zenith angle (Fig. 5), the increase is not dramatic. For HIRS/3 instruments with the 20-km PSF, the effect is even smaller, as the overall variance is reduced, and the geometry of the PSF matters less. Note, however, that we drop all points with a viewing angle above 40° before gridding in section 4.

The RMS differences between the HIRS T_b data and the corresponding AVHRR channel 4 T_b data (once it has been interpolated, shifted, and scaled) are below 1.6 K for the test data from 16 November 2009 (Table 1). Of these differences 70%–80% appear to be due to footprint-scale heterogeneity (Table 1, column 5; Fig. 6e), although some scene dependence is observed in smoothed RMS fields as well (Table 1, column 4; Fig. 6d).

Once we have determined the PSF for a given satellite, the AVHRR and CLAVR-x data are interpolated onto the HIRS grid as follows. The data are collocated using several rounds of elimination for purposes of computational speed:

1) For each row of HIRS, ignore all but the nearest 50 rows of AVHRR data.
2) For each HIRS footprint along the previously selected row:
    (i) Ignore all but the nearest 50 columns of AVHRR data.
    (ii) Ignore all but the AVHRR data within about 33 km in both the zonal and meridional directions.
    (iii) Ignore all but the AVHRR data within 20-km great-circle distance.

We then apply the conical PSF on AVHRR data within 20 km of the center of the HIRS footprint. Weights add to 1.0 by construction, so the shape of the PSF can change; for example, missing data near the center of the HIRS footprint may effectively result in an annular PSF. Typically, about 11 AVHRR pixels receive a nonzero weight.

These weights are applied in order to average AVHRR radiances and cloud types. However, averaging cloud type data from CLAVR-x (section 2), which consist of integers representing different cloud types, is not completely straightforward. Rather, we treat each possible cloud type as a separate Boolean field with each AVHRR pixel having a value of True (1) or False (0) for that cloud type. This field is multiplied by the weights from the PSF created to produce a floating point value between 0.0 and 1.0 for each HIRS footprint that could be considered a crude cloud fraction. Using this fuzzy logic approach, each HIRS footprint is assigned not merely a cloud type but an estimated cloud fraction corresponding to each cloud type.

4. Cloud type histograms and spatial gridding

Our second objective is to grid the cloud-characterized data onto latitude-longitude space. To preserve the statistical moments of the data in a computationally feasible manner, a single-pass statistical moment calculation algorithm based on Choi and Sweetman (2010) is employed that allows for efficient generation of statistics on arbitrarily long satellite data records. A T_b histogram for each

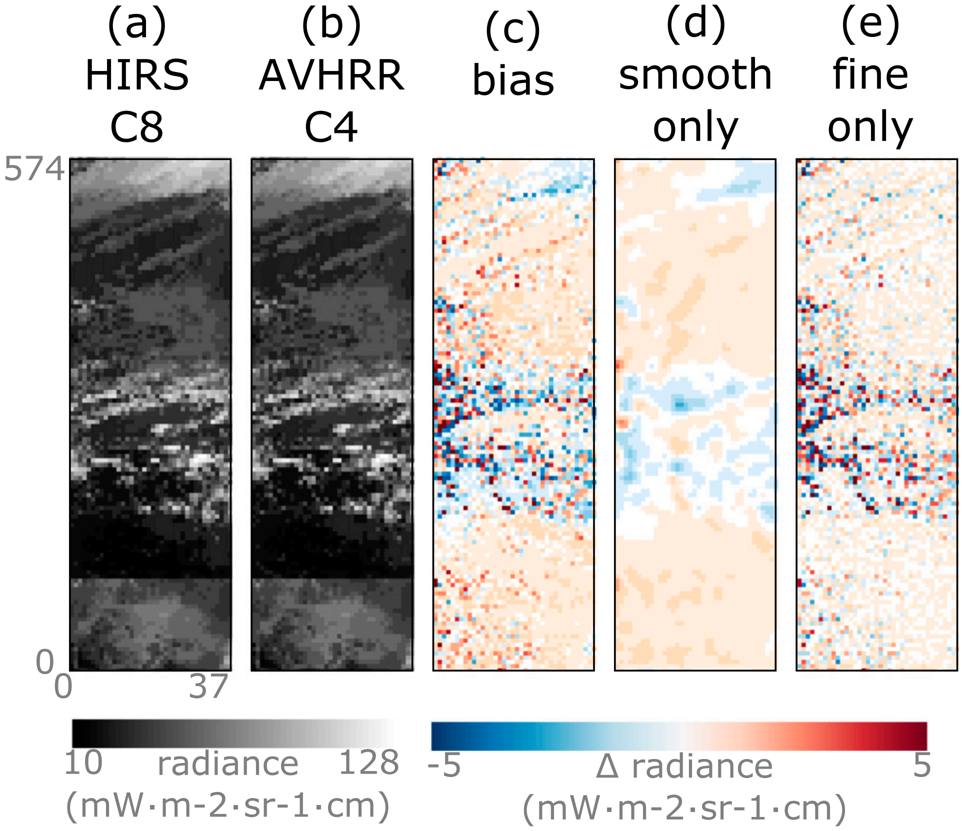

FIG. 6. (a) HIRS channel 8 radiances from *N19* for an ascending track over the northeastern Pacific on 16 Nov 2009. (b) AVHRR channel 4 radiances averaged onto HIRS footprints using the conical PSF, after the adjustment steps outlined in section 3. (c) AVHRR–HIRS biases for each footprint. (d) Biases after each field are Gaussian smoothed to remove footprint-scale heterogeneity. (e) Footprint-scale biases once the smooth fields have been removed.

channel, cloud type, and 1° × 1° longitude–latitude bin is produced, and the statistical moments are calculated based on the histograms. Example histograms for the northeast Pacific Ocean (−180°–120° longitude, 0°–40° latitude) are shown in Fig. 7. Calculating the statistics based on histograms amounts to calculating statistics based on weighted data, with the T_b bins serving as the values and the counts in each bin serving as the weights.

An advantage of this method is that calculating statistics for a region involves merely summing the histograms over longitude and latitude prior to the calculation of the statistics. This also lends itself to a straightforward method to account for the effect of sampling: before summing histograms, histograms from overrepresented bins are weighed less. This still makes use of all the satellite data available, but it produces the statistically expected sampling-corrected regional histogram (it also means that fractional counts are possible in histograms and maps, as in Figs. 7, 8).

While binning in longitude and latitude is straightforward, binning by cloud type is not as clear. In this study, the HIRS T_b that represents a given cloud type bin is counted if and only if the cloud type value within the HIRS footprint covers at least 90% of the footprint in question. If pixels are too heterogeneous to meet this qualification, then they are labeled as *other* to distinguish them from the *mixed* cloud type classification defined in CLAVR-x. This other classification is distinct from the *mixed* cloud classification; the former is a result of our interpolation, while the latter is based on a physical retrieval. An alternative fuzzy logic approach is to count all pixels, adding the fractional counts for each cloud type to the T_b histogram for that cloud type. This method avoids dismissing HIRS pixels as *other* and produces very similar results, except that even a slight contamination of high-cloud bins with T_b values from partial-low-cloud HIRS pixels results in as much as 6-K warming for high, convective, and overlapping cloud types.

While our method works for the entire globe, the methodology is tested over the northeast Pacific Ocean during a significant variation in ENSO. This region contains a wide variety of cloud types. Schreier et al. (2014) use cloud types

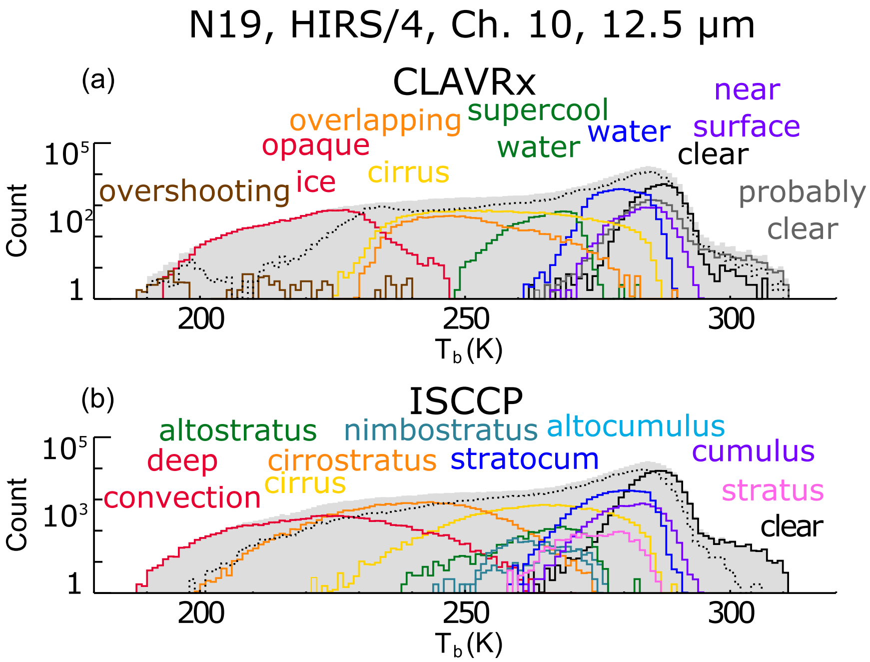

FIG. 7. *NOAA-19* HIRS/4 T_b histogram by (a) CLAVR-x and (b) ISCCP cloud type, as shown, during SOND 2009 over the northeast Pacific Ocean. The light gray envelope shows T_b counts for all cloud types. Note the logarithmic scale. Colors for CLAVR-x and ISCCP cloud types are chosen qualitatively to match in order to aid visual comparison between the two panels.

defined by the MODIS instrument to characterize AIRS hyperspectral infrared radiances within this region. The GEWEX Cloud System Study (GCSS) Pacific Cross-Section Intercomparison (GPCI) transect (Karlsson et al. 2010; Teixeira et al. 2011) is also located here and is a key region of focus for climate GCM evaluation.

During 15 September–15 December (SOND) 2009, cloud types in this region are dominated by marine stratocumulus in the northeast (CLAVR-x water or ISCCP stratocumulus in Fig. 8), and deep convective clouds (CLAVR-x opaque ice or ISCCP deep convection) and cirrus nearer to the equator. The moderate counts and the realistic distribution of sampling-corrected counts for various cloud types suggest that, while requiring a 10-km footprint to be nearly completely "covered" by a given cloud type may be a strict criterion for some cloud types (particularly the CLAVR-x *overshooting* type), the binning routine retains enough cloud counts to realistically represent cloud spatial distributions that can eventually be compared to EOS *Aqua* AIRS and MODIS observations. Further investigation on how to interpret the other type category within HIRS footprints warrants further investigation.

5. Case study in the northeast Pacific Ocean

Our third objective is to demonstrate the strengths and weaknesses of the previously described methods for quantifying specific aspects of climate variability with the HIRS–AVHRR record. Toward this end, a case study of cloud type T_b variability over the northeast Pacific Ocean region is described and investigated. In section 5a, the mean and standard deviation from a selected NOAA satellite are described, noting that these statistics can be generalized to the other satellites of interest. Then, the differences in statistics between pairs of satellites or between years are shown.

Next, pairs of distributions from multiple satellites or time periods are examined. In section 5b, the late 2009 overlap between *N18* and *N19* is described and involves two satellites with nearly identical configurations with AVHRR/3 and HIRS/4 instruments. In section 5c, the early 2014 overlaps between *N16* and the two MetOp satellites allow a comparison between HIRS/3 and HIRS/4. *N16* carries the ~20-km HIRS/3 and *M1* carries the ~10-km HIRS/4. In section 5d, we sample two times during the diurnal cycle using *M2* and *N19*. In section 5e, we describe differences associated with ENSO variability using *N18* and *M2* data between 2008 and 2009. The ECTs of the two satellites are steady during this period, while the tropical Pacific transitions from a La Niña state to an El Niño state.

a. Radiance statistics

As a first check of our methods, the mean values of spectral T_b for *N19* during SOND 2009 are shown in

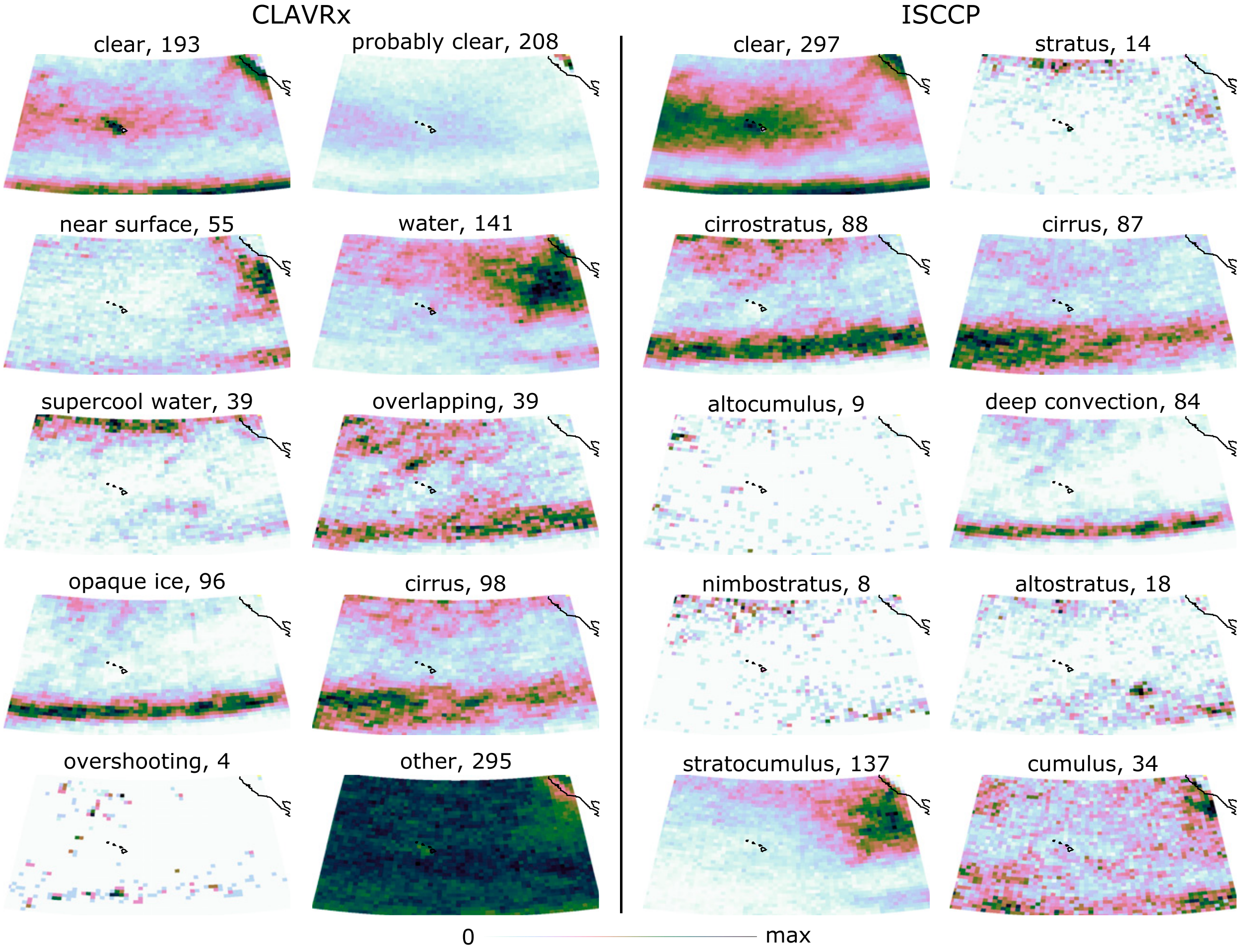

FIG. 8. Sampling-corrected *N18* cloud type frequency during SOND 2009 over the northeast Pacific Ocean. Scales for each panel range from 0 (white) to the number shown at the top of each panel (black). Counts by cloud type are divided by source, with CLAVR-x cloud types in the left two columns and ISCCP cloud types in the right two columns. The color scale is from Green (2011).

Fig. 9. Even though HIRS pixels with a mix of AVHRR cloud types are not considered here, HIRS pixels are still identified as containing a specific CLAVR-x cloud type 46% of the time and ISCCP cloud type 51% of the time. Examining T_b by channel, we observe that T_b generally increase with wavenumbers throughout the CO_2-slicing channels, peaking in magnitude in the window channels centered at 12.5 and 11.1 μm. Brightness temperatures are lower within the water vapor and O_3 bands. Brightness temperatures decrease with wavelength in the N_2O and CO_2 bands in the shortwave IR, and again increase in the shortwave IR window near 3.7 μm. The spectral dependence is entirely consistent with our knowledge of the mid-IR spectrum.

Examining T_b by cloud type, high clouds (Fig. 9, brown, red, orange, and yellow) generally exhibit lower T_b as expected, although the cirrus cloud type (Fig. 9, yellow) has a higher T_b because of its low opacity. Overlapping clouds (Fig. 9a, orange) likewise have a fairly high T_b since their observed T_b include components due to multiple layers of clouds within those pixels. Overshooting clouds (Fig. 9a, brown) stand out as the coldest cloud type since they occur in proximity to the cold-point tropopause and are opaque to IR wavelengths. CLAVR-x cloud types generally produce more distinct spectral separation in the histograms (Figs. 9a, 7a) than ISCCP cloud types (Figs. 9b, 7b).

CLAVR-x distinguishes between ice and water phases in clouds with $T_b < 273$ K. Ice clouds are more absorptive than water clouds in the 11–12.5-μm channels, but from 11 to 12.5 μm, the absorption by water clouds increases more rapidly than the absorption by ice clouds (Strabala et al. 1994; Nasiri and Kahn 2008; Jin and Nasiri 2014; Kahn et al. 2014). This difference between phases is inferred by the steepness of the slopes

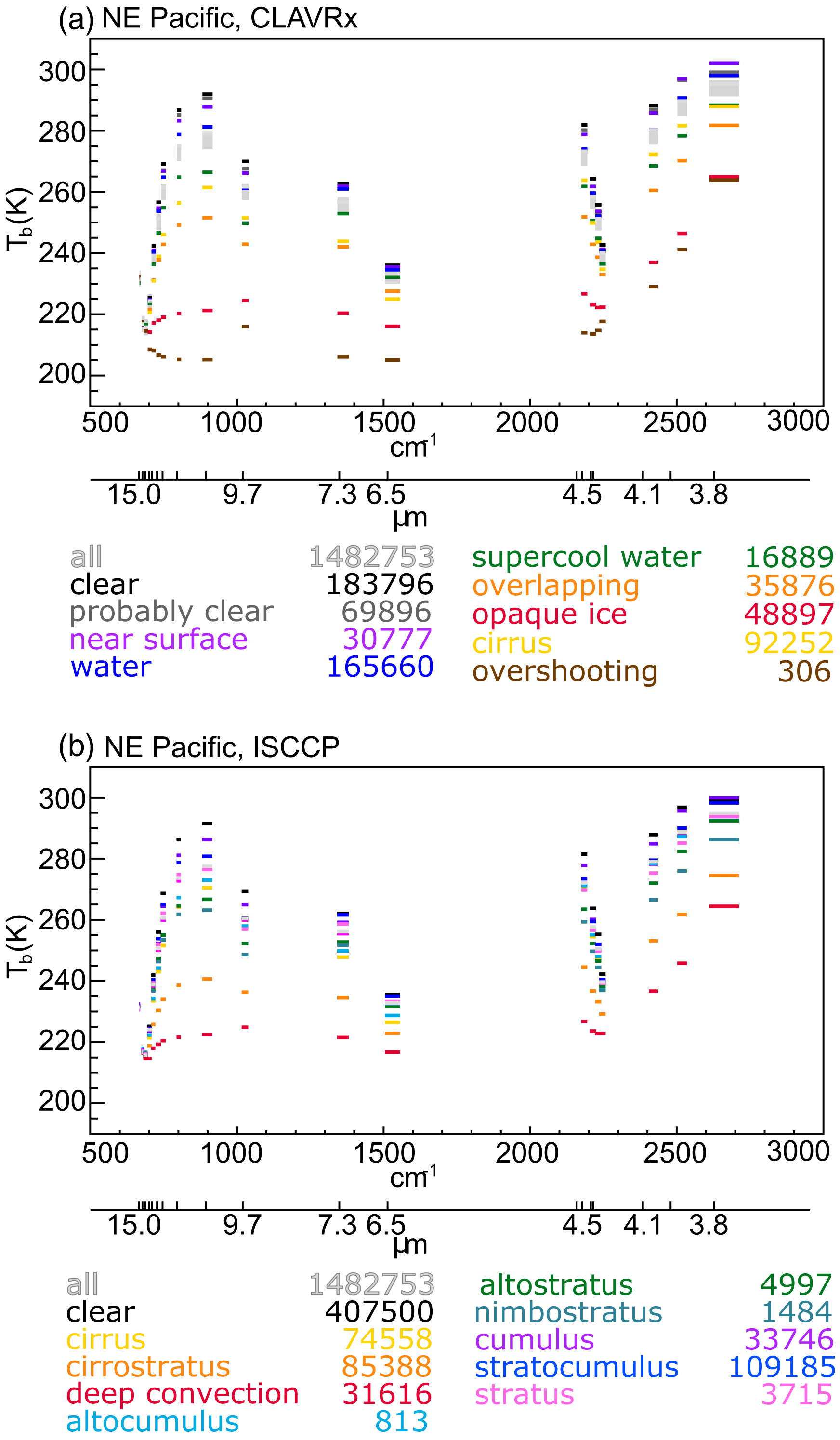

FIG. 9. Brightness temperatures T_b as a function of channel wavelength for the 19 infrared *N19* HIRS/4 channels during SOND 2009, for (a) CLAVR-x cloud types and (b) ISCCP cloud types, by color. Total HIRS footprint counts for each cloud type are listed below each panel. Cloud types in the other category are omitted for clarity, although their statistics are close to those for all cloud types.

(a) SOND 2009 N18 mean T_b

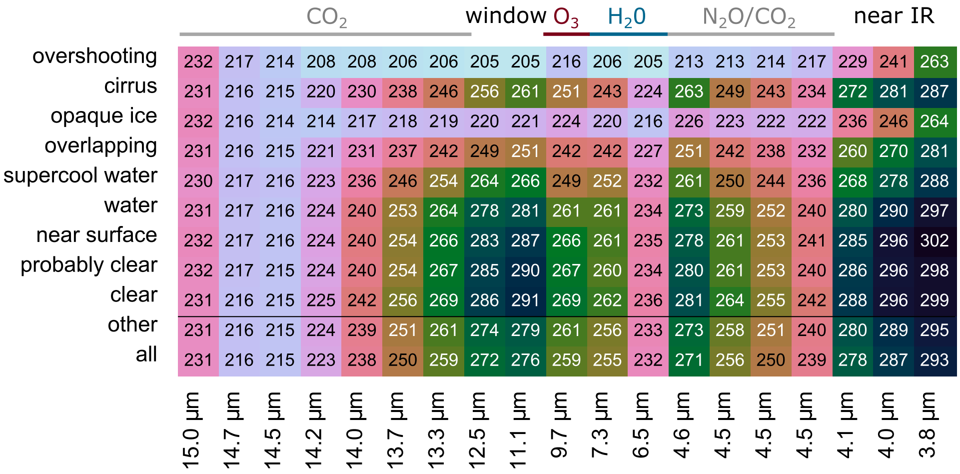

	15.0 µm	14.7 µm	14.5 µm	14.2 µm	14.0 µm	13.7 µm	13.3 µm	12.5 µm	11.1 µm	9.7 µm	7.3 µm	6.5 µm	4.6 µm	4.5 µm	4.5 µm	4.5 µm	4.1 µm	4.0 µm	3.8 µm
overshooting	232	217	214	208	208	206	206	205	205	216	206	205	213	213	214	217	229	241	263
cirrus	231	216	215	220	230	238	246	256	261	251	243	224	263	249	243	234	272	281	287
opaque ice	232	216	214	214	217	218	219	220	221	224	220	216	226	223	222	222	236	246	264
overlapping	231	216	215	221	231	237	242	249	251	242	242	227	251	242	238	232	260	270	281
supercool water	230	217	216	223	236	246	254	264	266	249	252	232	261	250	244	236	268	278	288
water	231	217	216	224	240	253	264	278	281	261	261	234	273	259	252	240	280	290	297
near surface	232	217	216	224	240	254	266	283	287	266	261	235	278	261	253	241	285	296	302
probably clear	232	217	215	224	240	254	267	285	290	267	260	234	280	261	253	240	286	296	298
clear	231	216	215	225	242	256	269	286	291	269	262	236	281	264	255	242	288	296	299
other	231	216	215	224	239	251	261	274	279	261	256	233	273	258	251	240	280	289	295
all	231	216	215	223	238	250	259	272	276	259	255	232	271	256	250	239	278	287	293

(b) SOND 2009 N18 T_b standard deviation

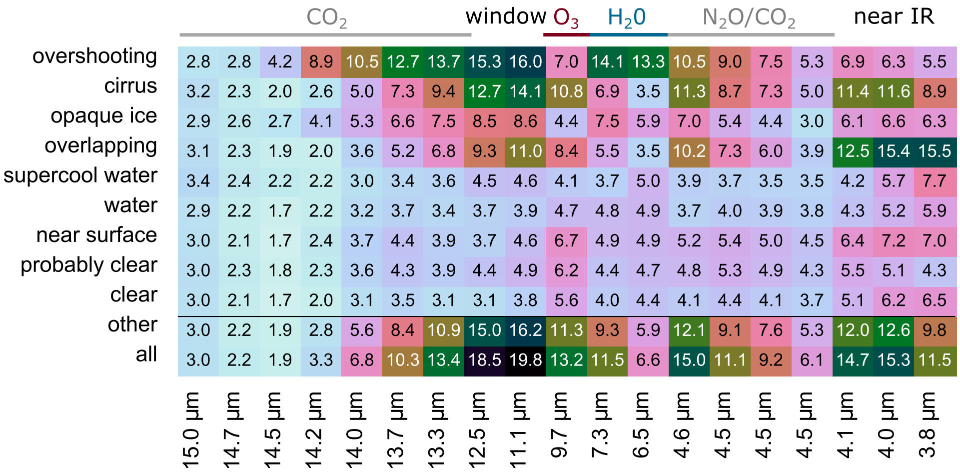

	15.0 µm	14.7 µm	14.5 µm	14.2 µm	14.0 µm	13.7 µm	13.3 µm	12.5 µm	11.1 µm	9.7 µm	7.3 µm	6.5 µm	4.6 µm	4.5 µm	4.5 µm	4.5 µm	4.1 µm	4.0 µm	3.8 µm
overshooting	2.8	2.8	4.2	8.9	10.5	12.7	13.7	15.3	16.0	7.0	14.1	13.3	10.5	9.0	7.5	5.3	6.9	6.3	5.5
cirrus	3.2	2.3	2.0	2.6	5.0	7.3	9.4	12.7	14.1	10.8	6.9	3.5	11.3	8.7	7.3	5.0	11.4	11.6	8.9
opaque ice	2.9	2.6	2.7	4.1	5.3	6.6	7.5	8.5	8.6	4.4	7.5	5.9	7.0	5.4	4.4	3.0	6.1	6.6	6.3
overlapping	3.1	2.3	1.9	2.0	3.6	5.2	6.8	9.3	11.0	8.4	5.5	3.5	10.2	7.3	6.0	3.9	12.5	15.4	15.5
supercool water	3.4	2.4	2.2	2.2	3.0	3.4	3.6	4.5	4.6	4.1	3.7	5.0	3.9	3.7	3.5	3.5	4.2	5.7	7.7
water	2.9	2.2	1.7	2.2	3.2	3.7	3.4	3.7	3.9	4.7	4.8	4.9	3.7	4.0	3.9	3.8	4.3	5.2	5.9
near surface	3.0	2.1	1.7	2.4	3.7	4.4	3.9	3.7	4.6	6.7	4.9	4.9	5.2	5.4	5.0	4.5	6.4	7.2	7.0
probably clear	3.0	2.3	1.8	2.3	3.6	4.3	3.9	4.4	4.9	6.2	4.4	4.7	4.8	5.3	4.9	4.3	5.5	5.1	4.3
clear	3.0	2.1	1.7	2.0	3.1	3.5	3.1	3.1	3.8	5.6	4.0	4.4	4.1	4.4	4.1	3.7	5.1	6.2	6.5
other	3.0	2.2	1.9	2.8	5.6	8.4	10.9	15.0	16.2	11.3	9.3	5.9	12.1	9.1	7.6	5.3	12.0	12.6	9.8
all	3.0	2.2	1.9	3.3	6.8	10.3	13.4	18.5	19.8	13.2	11.5	6.6	15.0	11.1	9.2	6.1	14.7	15.3	11.5

FIG. 10. HIRS/4 (a) mean T_b and (b) σT_b statistics over the northeast Pacific by cloud type and channel during SOND 2009 for *N18*. Cells are shaded according to the value printed in the cell.

connecting the 11- and 12.5-μm T_b for different cloud types. CLAVR-x opaque ice (Fig. 9a, red) and overlapping (Fig. 9a, brown), and the ISCCP deep convection (Fig. 9b, red) T_b decrease very little from 11.1 to 12.5 μm compared to warmer cloud types.

Before discussing T_b standard deviations (σT_b), we call the reader's attention to Fig. 10a. This figure presents nearly the same information as Fig. 9a but in a grid format that allows for direct comparison between the mean T_b and σT_b (Fig. 10b). The σT_b are reduced for low-cloud types (Fig. 10b, lower rows) and are generally elevated for high-cloud types (on the order of 10 K; Fig. 10b, upper rows), since high clouds have a larger thermal contrast. The high standard deviations for the water vapor channels for overshooting cloud types may also be related to the presence of highly variable water vapor at otherwise very dry altitudes. Dimensional analysis suggests that fractional differences in air temperature between neighboring HIRS pixels are typically within 10%, whereas water vapor can vary strongly between a convective column and the surrounding dry air (Soden et al. 2005). Indeed, AIRS water vapor channel σT_b is large in the tropics compared to higher latitudes, while actual temperature standard deviation is small in these regions (Kahn and Teixeira 2009). Therefore, we speculate that the proportionally high σT_b in the H_2O channels may be related not only to cloud variability, but perhaps to water vapor variability associated with a convective environment.

The high standard deviation of cirrus clouds in the O_3 channel is not surprising, since cirrus clouds are understood to contaminate O_3 retrievals in the 9.6-μm band (Joiner et al. 1998). The σT_b for this channel, then, include contributions from O_3 and cirrus clouds over a

(a) SOND 2009 N19 – N18 mean T_b

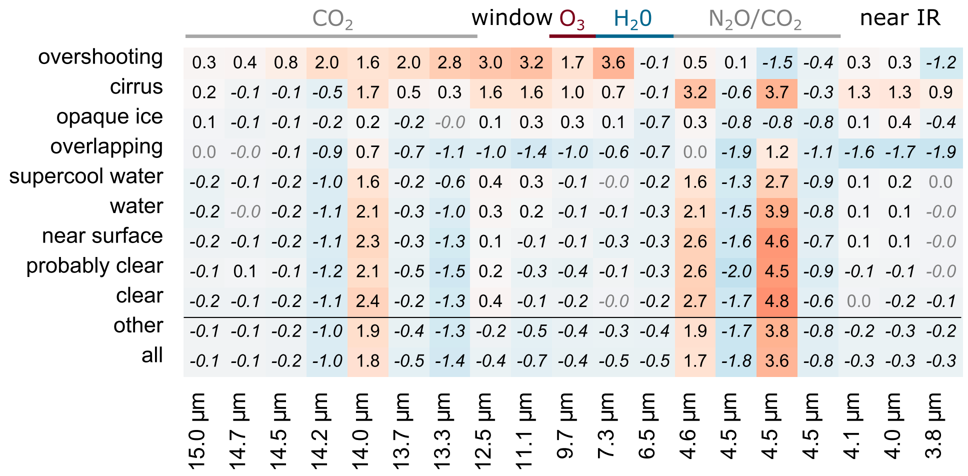

	CO_2							window		O_3	H_20		N_2O/CO_2				near IR		
	15.0 μm	14.7 μm	14.5 μm	14.2 μm	14.0 μm	13.7 μm	13.3 μm	12.5 μm	11.1 μm	9.7 μm	7.3 μm	6.5 μm	4.6 μm	4.5 μm	4.5 μm	4.5 μm	4.1 μm	4.0 μm	3.8 μm
overshooting	0.3	0.4	0.8	2.0	1.6	2.0	2.8	3.0	3.2	1.7	3.6	-0.1	0.5	0.1	-1.5	-0.4	0.3	0.3	-1.2
cirrus	0.2	-0.1	-0.1	-0.5	1.7	0.5	0.3	1.6	1.6	1.0	0.7	-0.1	3.2	-0.6	3.7	-0.3	1.3	1.3	0.9
opaque ice	0.1	-0.1	-0.1	-0.2	0.2	-0.2	-0.0	0.1	0.3	0.3	0.1	-0.7	0.3	-0.8	-0.8	-0.8	0.1	0.4	-0.4
overlapping	0.0	-0.0	-0.1	-0.9	0.7	-0.7	-1.1	-1.0	-1.4	-1.0	-0.6	-0.7	0.0	-1.9	1.2	-1.1	-1.6	-1.7	-1.9
supercool water	-0.2	-0.1	-0.2	-1.0	1.6	-0.2	-0.6	0.4	0.3	-0.1	-0.0	-0.2	1.6	-1.3	2.7	-0.9	0.1	0.2	0.0
water	-0.2	-0.0	-0.2	-1.1	2.1	-0.3	-1.0	0.3	0.2	-0.1	-0.1	-0.3	2.1	-1.5	3.9	-0.8	0.1	0.1	-0.0
near surface	-0.2	-0.1	-0.2	-1.1	2.3	-0.3	-1.3	0.1	-0.1	-0.1	-0.3	-0.3	2.6	-1.6	4.6	-0.7	0.1	0.1	-0.0
probably clear	-0.1	0.1	-0.1	-1.2	2.1	-0.5	-1.5	0.2	-0.3	-0.4	-0.1	-0.3	2.6	-2.0	4.5	-0.9	-0.1	-0.1	-0.0
clear	-0.2	-0.1	-0.2	-1.1	2.4	-0.2	-1.3	0.4	-0.1	-0.2	-0.0	-0.2	2.7	-1.7	4.8	-0.6	0.0	-0.2	-0.1
other	-0.1	-0.1	-0.2	-1.0	1.9	-0.4	-1.3	-0.2	-0.5	-0.4	-0.3	-0.4	1.9	-1.7	3.8	-0.8	-0.2	-0.3	-0.2
all	-0.1	-0.1	-0.2	-1.0	1.8	-0.5	-1.4	-0.4	-0.7	-0.4	-0.5	-0.5	1.7	-1.8	3.6	-0.8	-0.3	-0.3	-0.3

(b) SOND 2009 N19 ÷ N18 T_b variances

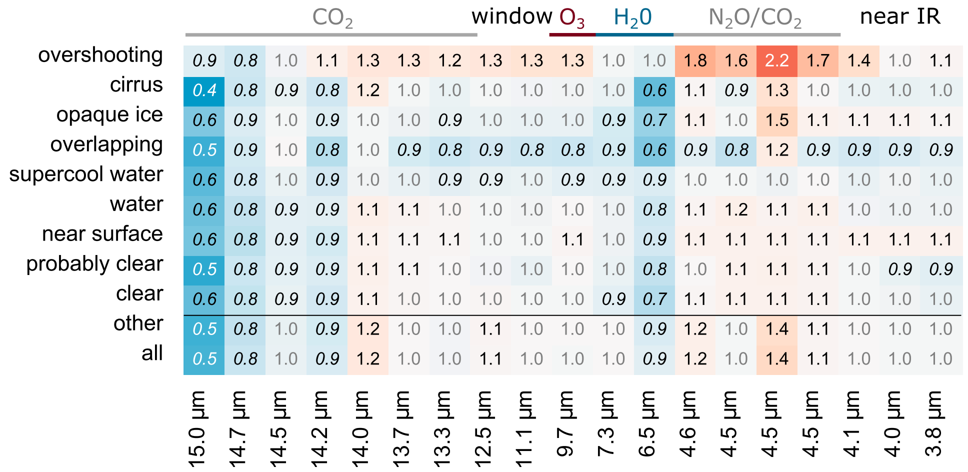

	CO_2							window		O_3	H_20		N_2O/CO_2				near IR		
	15.0 μm	14.7 μm	14.5 μm	14.2 μm	14.0 μm	13.7 μm	13.3 μm	12.5 μm	11.1 μm	9.7 μm	7.3 μm	6.5 μm	4.6 μm	4.5 μm	4.5 μm	4.5 μm	4.1 μm	4.0 μm	3.8 μm
overshooting	0.9	0.8	1.0	1.1	1.3	1.3	1.2	1.3	1.3	1.3	1.0	1.0	1.8	1.6	2.2	1.7	1.4	1.0	1.1
cirrus	0.4	0.8	0.9	0.8	1.2	1.0	1.0	1.0	1.0	1.0	1.0	0.6	1.1	0.9	1.3	1.0	1.0	1.0	1.0
opaque ice	0.6	0.9	1.0	0.9	1.0	1.0	0.9	1.0	1.0	1.0	0.9	0.7	1.1	1.0	1.5	1.1	1.1	1.1	1.1
overlapping	0.5	0.9	1.0	0.8	1.0	0.9	0.8	0.9	0.8	0.8	0.9	0.6	0.9	0.8	1.2	0.9	0.9	0.9	0.9
supercool water	0.6	0.8	1.0	0.9	1.0	1.0	0.9	0.9	1.0	0.9	0.9	0.9	1.0	1.0	1.0	1.0	1.0	1.0	1.0
water	0.6	0.8	0.9	0.9	1.1	1.1	1.0	1.0	1.0	1.0	1.0	0.8	1.1	1.2	1.1	1.1	1.0	1.0	1.0
near surface	0.6	0.8	0.9	0.9	1.1	1.1	1.1	1.0	1.0	1.1	1.0	0.9	1.1	1.1	1.1	1.1	1.1	1.1	1.1
probably clear	0.5	0.8	0.9	0.9	1.1	1.1	1.0	1.0	1.0	1.0	1.0	0.8	1.0	1.1	1.1	1.1	1.0	0.9	0.9
clear	0.6	0.8	0.9	0.9	1.1	1.0	1.0	1.0	1.0	1.0	0.9	0.7	1.1	1.1	1.1	1.1	1.0	1.0	1.0
other	0.5	0.8	1.0	0.9	1.2	1.0	1.0	1.1	1.0	1.0	1.0	0.9	1.2	1.0	1.4	1.1	1.0	1.0	1.0
all	0.5	0.8	1.0	0.9	1.2	1.0	1.0	1.1	1.0	1.0	1.0	0.9	1.2	1.0	1.4	1.1	1.0	1.0	1.0

FIG. 11. As in Fig. 10, but for (a) *N19* minus *N18* ΔT_b and (b) *N19* divided by *N18* $\sigma^2 T_b$ statistics. Warm colors in the right-hand column denote (a) warmer *N19* T_b and (b) higher *N19* $\sigma^2 T_b$. Negative values are italicized. Cells are shaded according to the value printed in the cell.

large region with diverse cloud regimes. Heterogeneous scenes, labeled as other, also show elevated standard deviations, consistent with the mixing of multiple cloud types.

In summary, the cloud type– and channel-specific T_b statistics are realistic and are consistent with basic knowledge of the cloudy mid-IR emission spectrum, validating both the cloud typing and gridding methodologies.

b. *Intersatellite differences*

To apply our methods to study variability and change, we first need to characterize the differences between satellites analyzing the same—or nearly the same—scene. We thus begin our comparisons by considering two satellites (*N18* and *N19*) with nearly identical AVHRR/3 and HIRS/4 instrument combinations and the same ECT at 1330 LST (Fig. 11). The mean T_b biases between the two instruments are mostly small and $\leq \pm 1$ K (Fig. 11a), although *N19* T_b are as much as 4 K warmer in the CO_2-slicing channels for all cloud types. This is in agreement with Shi et al. (2008), who find that scene-dependent radiance biases can be larger than 1 K within an individual channel and arise from a small shift in central wavenumber (Chen et al. 2013; Shi and Bates 2011). Chen et al. (2013) account for intersatellite shifts in spectral response functions using a multichannel linear fit and achieve very close consistency (within about ±1 K) for the 14–15-μm CO_2-slicing channels. Our work highlights the need for further intercalibration efforts for other channels as well.

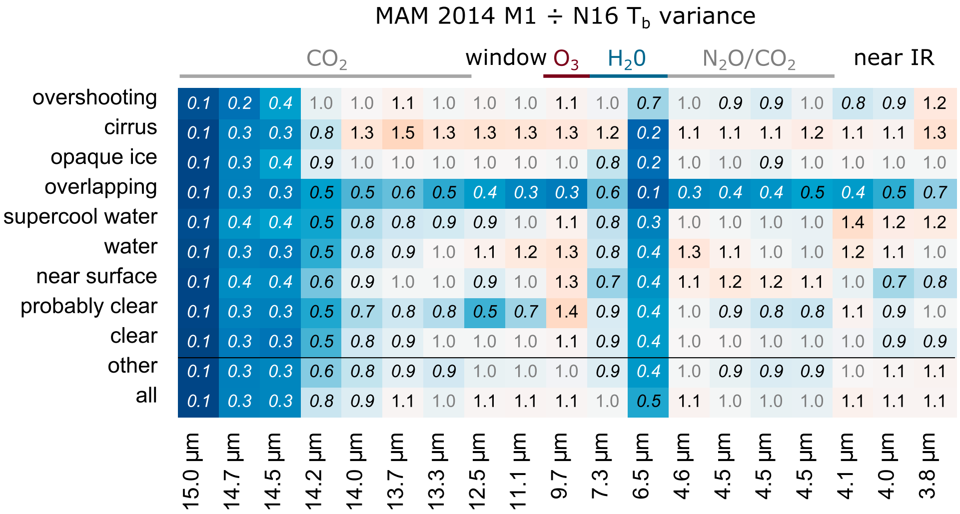

	15.0 µm	14.7 µm	14.5 µm	14.2 µm	14.0 µm	13.7 µm	13.3 µm	12.5 µm	11.1 µm	9.7 µm	7.3 µm	6.5 µm	4.6 µm	4.5 µm	4.5 µm	4.5 µm	4.1 µm	4.0 µm	3.8 µm
overshooting	*0.1*	*0.2*	*0.4*	1.0	1.0	1.1	1.0	1.0	1.0	1.1	1.0	*0.7*	1.0	*0.9*	*0.9*	1.0	*0.8*	*0.9*	1.2
cirrus	*0.1*	*0.3*	*0.3*	*0.8*	1.3	1.5	1.3	1.3	1.3	1.3	1.2	*0.2*	1.1	1.1	1.1	1.2	1.1	1.1	1.3
opaque ice	*0.1*	*0.3*	*0.4*	*0.9*	1.0	1.0	1.0	1.0	1.0	1.0	*0.8*	*0.2*	1.0	1.0	*0.9*	1.0	1.0	1.0	1.0
overlapping	*0.1*	*0.3*	*0.3*	*0.5*	*0.5*	*0.6*	*0.5*	*0.4*	*0.3*	*0.3*	*0.6*	*0.1*	*0.3*	*0.4*	*0.4*	*0.5*	*0.4*	*0.5*	*0.7*
supercool water	*0.1*	*0.4*	*0.4*	*0.5*	*0.8*	*0.8*	*0.9*	*0.9*	1.0	1.1	*0.8*	*0.3*	1.0	1.0	1.0	1.0	1.4	1.2	1.2
water	*0.1*	*0.3*	*0.3*	*0.5*	*0.8*	*0.9*	1.0	1.1	1.2	1.3	*0.8*	*0.4*	1.3	1.1	1.0	1.0	1.2	1.1	1.0
near surface	*0.1*	*0.4*	*0.4*	*0.6*	*0.9*	1.0	1.0	*0.9*	1.0	1.3	*0.7*	*0.4*	1.1	1.2	1.2	1.1	1.0	*0.7*	*0.8*
probably clear	*0.1*	*0.3*	*0.3*	*0.5*	*0.7*	*0.8*	*0.8*	*0.5*	*0.7*	1.4	*0.9*	*0.4*	1.0	*0.9*	*0.8*	*0.8*	1.1	*0.9*	1.0
clear	*0.1*	*0.3*	*0.3*	*0.5*	*0.8*	*0.9*	1.0	1.0	1.0	1.1	*0.9*	*0.4*	1.0	1.0	1.0	1.0	1.0	*0.9*	*0.9*
other	*0.1*	*0.3*	*0.3*	*0.6*	*0.8*	*0.9*	*0.9*	1.0	1.0	1.0	*0.9*	*0.4*	1.0	*0.9*	*0.9*	*0.9*	1.0	1.1	1.1
all	*0.1*	*0.3*	*0.3*	*0.8*	*0.9*	1.1	1.0	1.1	1.1	1.1	1.0	*0.5*	1.1	1.0	1.0	1.0	1.1	1.1	1.1

FIG. 12. *M1* HIRS/4 divided by *N16* HIRS/3 $\sigma^2 T_b$ statistics over the northeast Pacific by cloud type during MAM 2014. Warm colors denote higher *M1* $\sigma^2 T_b$. Negative values are italicized. Cells are shaded according to the value printed in the cell.

While shifts in the spectral response function for tropospheric slicing channels yield different biases for different cloud types, the shifts have larger effects on cloud types at an altitude at or above the peak of the vertical weighting function for a given channel. In contrast, T_b biases for the 14–11-μm bands are small for opaque ice cloud types that are located well above the weighting function altitudes for these channels.

Window channels are not as susceptible to spectral response function shifts, but they still show an overall cold bias from *N18* to *N19*. Interestingly, cloud type–specific biases for most types are smaller than the overall mean bias. With similar viewing geometry, and an ECT difference of only minutes on top of an already small diurnal cycle, the existence of such an overall bias between these channels is intriguing.

Cloud type–specific biases that span multiple columns are likely caused by systematic differences in intersatellite CLAVR-x cloud typing. Corresponding biases for ISCCP cloud types (not shown) do not exhibit strong intersatellite cloud type–specific bias differences. This does not necessarily disadvantage the CLAVR-x cloud typing since ISCCP cloud type categories are less distinct from each other than those from the CLAVR-x.

From HIRS status reports (e.g., Fig. 1), a decrease in noise is expected for *N19* relative to *N18*. The $\sigma^2 T_b$ are indeed lower for channels 1–4 (14.2–15.0 μm) and channel 12 (6.5 μm) for *N19* than for *N18* (Fig. 11b). For other channels, $\sigma^2 T_b$ ratios are very near unity, or even positive. The increase in σT_b of overshooting clouds is possibly due to sampling, because of the short lifetime, small scale, and low counts for this cloud type. However, cirrus, opaque ice, and overlapping cloud counts are high for both satellites. Thus, the decreasing $\sigma^2 T_b$ values across channels for these cloud types are likely due to differences in CLAVR-x cloud typing between *N18* and *N19*.

In summary, intersatellite biases are within ±1 K for most channels and cloud types, although several channels have notable biases for some cloud types (e.g., overshooting and cirrus, and overlapping) and channels (e.g., the slicing, N_2O, and CO_2 channels). The horizontal banding in Fig. 11a indicates biases due to AVHRR or CLAVR-x, while vertical banding indicates biases in HIRS. The $\sigma^2 T_b$ ratios of variances suggest reduced noise from *N18* to the newer *N19* satellite for several channels. Importantly, *N19* variance changes are within ±10% for most cloud types and channels.

c. *HIRS resolution changes*

Our gridding methodology is now used to examine differences in T_b statistics for HIRS/3 and HIRS/4 instruments, with resolutions of about 20 and 10 km, respectively. The *N16* and *M1* observations during 1 March–31 May (MAM) 2014 are used as the ECTs of the two instruments' overlap during this time period.

One may expect that the T_b distributions could differ for instruments of varying resolution. For instance, it is less likely that a 20-km footprint is covered by one cloud type than it is for a 10-km footprint. During MAM 2014, about a third of the pixels for *N16* are grouped under a specific cloud type (29% for CLAVR-x and 33% for ISCCP) compared with about half for *M1* (47% for CLAVR-x and 54% for ISCCP). Furthermore, standard

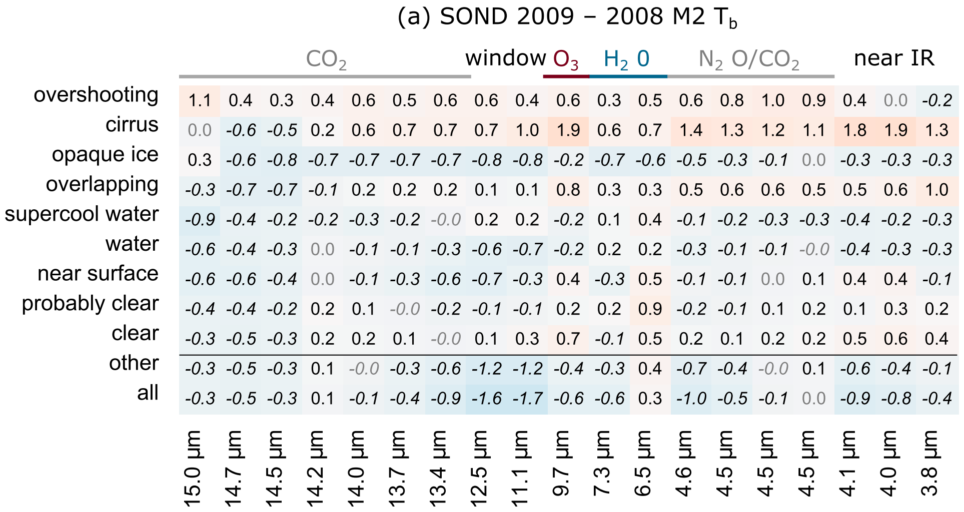

(a) SOND 2009 – 2008 M2 T_b

	CO_2							window		O_3	H_2 0		N_2 O/CO_2				near IR		
	15.0 µm	14.7 µm	14.5 µm	14.2 µm	14.0 µm	13.7 µm	13.4 µm	12.5 µm	11.1 µm	9.7 µm	7.3 µm	6.5 µm	4.6 µm	4.5 µm	4.5 µm	4.5 µm	4.1 µm	4.0 µm	3.8 µm
overshooting	1.1	0.4	0.3	0.4	0.6	0.5	0.6	0.6	0.4	0.6	0.3	0.5	0.6	0.8	1.0	0.9	0.4	0.0	*-0.2*
cirrus	0.0	*-0.6*	*-0.5*	0.2	0.6	0.7	0.7	0.7	1.0	1.9	0.6	0.7	1.4	1.3	1.2	1.1	1.8	1.9	1.3
opaque ice	0.3	*-0.6*	*-0.8*	*-0.7*	*-0.7*	*-0.7*	*-0.7*	*-0.8*	*-0.8*	*-0.2*	*-0.7*	*-0.6*	*-0.5*	*-0.3*	*-0.1*	0.0	*-0.3*	*-0.3*	*-0.3*
overlapping	*-0.3*	*-0.7*	*-0.7*	*-0.1*	0.2	0.2	0.2	0.1	0.1	0.8	0.3	0.3	0.5	0.6	0.6	0.5	0.5	0.6	1.0
supercool water	*-0.9*	*-0.4*	*-0.2*	*-0.2*	*-0.3*	*-0.2*	*-0.0*	0.2	0.2	*-0.2*	0.1	0.4	*-0.1*	*-0.2*	*-0.3*	*-0.3*	*-0.4*	*-0.2*	*-0.3*
water	*-0.6*	*-0.4*	*-0.3*	0.0	*-0.1*	*-0.1*	*-0.3*	*-0.6*	*-0.7*	*-0.2*	0.2	0.2	*-0.3*	*-0.1*	*-0.1*	*-0.0*	*-0.4*	*-0.3*	*-0.3*
near surface	*-0.6*	*-0.6*	*-0.4*	0.0	*-0.1*	*-0.3*	*-0.6*	*-0.7*	*-0.3*	0.4	*-0.3*	0.5	*-0.1*	*-0.1*	0.0	0.1	0.4	0.4	*-0.1*
probably clear	*-0.4*	*-0.4*	*-0.2*	0.2	0.1	*-0.0*	*-0.2*	*-0.1*	*-0.1*	0.2	0.2	0.9	*-0.2*	*-0.1*	0.1	0.2	0.1	0.3	0.2
clear	*-0.3*	*-0.5*	*-0.3*	0.2	0.2	0.1	*-0.0*	0.1	0.3	0.7	*-0.1*	0.5	0.2	0.1	0.2	0.2	0.5	0.6	0.4
other	*-0.3*	*-0.5*	*-0.3*	0.1	*-0.0*	*-0.3*	*-0.6*	*-1.2*	*-1.2*	*-0.4*	*-0.3*	0.4	*-0.7*	*-0.4*	*-0.0*	0.1	*-0.6*	*-0.4*	*-0.1*
all	*-0.3*	*-0.5*	*-0.3*	0.1	*-0.1*	*-0.4*	*-0.9*	*-1.6*	*-1.7*	*-0.6*	*-0.6*	0.3	*-1.0*	*-0.5*	*-0.1*	0.0	*-0.9*	*-0.8*	*-0.4*

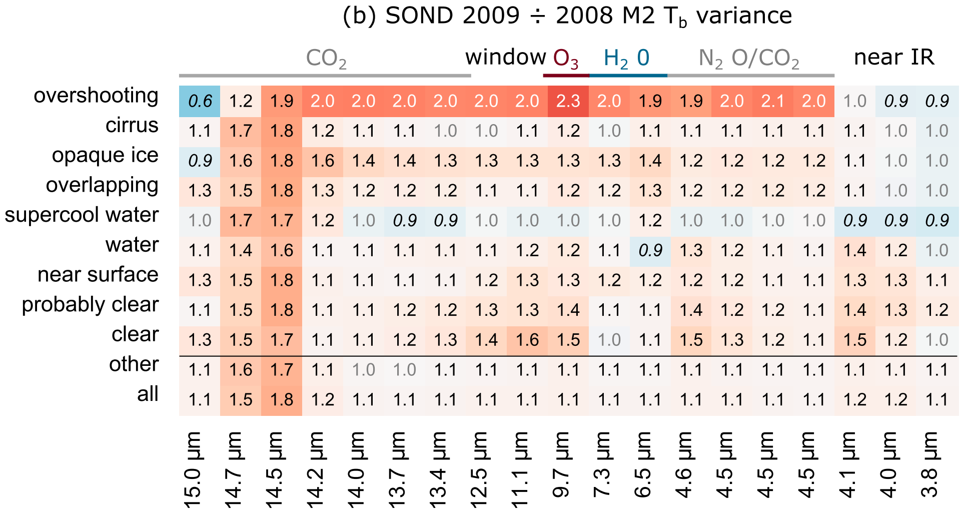

(b) SOND 2009 ÷ 2008 M2 T_b variance

	CO_2							window		O_3	H_2 0		N_2 O/CO_2				near IR		
	15.0 µm	14.7 µm	14.5 µm	14.2 µm	14.0 µm	13.7 µm	13.4 µm	12.5 µm	11.1 µm	9.7 µm	7.3 µm	6.5 µm	4.6 µm	4.5 µm	4.5 µm	4.5 µm	4.1 µm	4.0 µm	3.8 µm
overshooting	*0.6*	1.2	1.9	2.0	2.0	2.0	2.0	2.0	2.0	2.3	2.0	1.9	1.9	2.0	2.1	2.0	1.0	*0.9*	*0.9*
cirrus	1.1	1.7	1.8	1.2	1.1	1.1	1.0	1.0	1.1	1.2	1.0	1.1	1.1	1.1	1.1	1.1	1.1	1.0	1.0
opaque ice	*0.9*	1.6	1.8	1.6	1.4	1.4	1.3	1.3	1.3	1.3	1.3	1.4	1.2	1.2	1.2	1.2	1.1	1.0	1.0
overlapping	1.3	1.5	1.8	1.3	1.2	1.2	1.2	1.1	1.1	1.2	1.2	1.3	1.2	1.2	1.2	1.2	1.1	1.0	1.0
supercool water	1.0	1.7	1.7	1.2	1.0	*0.9*	*0.9*	1.0	1.0	1.0	1.0	1.2	1.0	1.0	1.0	1.0	*0.9*	*0.9*	*0.9*
water	1.1	1.4	1.6	1.1	1.1	1.1	1.1	1.1	1.2	1.2	1.1	*0.9*	1.3	1.2	1.1	1.1	1.4	1.2	1.0
near surface	1.3	1.5	1.8	1.1	1.1	1.1	1.1	1.2	1.3	1.3	1.2	1.2	1.2	1.2	1.1	1.1	1.3	1.3	1.1
probably clear	1.1	1.5	1.8	1.1	1.1	1.2	1.2	1.3	1.3	1.4	1.1	1.1	1.4	1.2	1.2	1.1	1.4	1.3	1.2
clear	1.3	1.5	1.7	1.1	1.1	1.2	1.3	1.4	1.6	1.5	1.0	1.1	1.5	1.3	1.2	1.1	1.5	1.2	1.0
other	1.1	1.6	1.7	1.1	1.0	1.0	1.1	1.1	1.1	1.1	1.1	1.1	1.1	1.1	1.1	1.1	1.1	1.1	1.1
all	1.1	1.5	1.8	1.2	1.1	1.1	1.1	1.1	1.1	1.1	1.1	1.1	1.1	1.1	1.1	1.1	1.2	1.2	1.1

FIG. 13. As in Fig. 11, but for (a) 2009 minus 2008 ΔT_b and (b) 2009 divided by 2008 $\sigma^2 T_b$ statistics for *M2* during SOND. Warm colors denote (a) warmer 2009 T_b and (b) higher 2009 $\sigma^2 T_b$. Negative values are italicized. Cells are shaded according to the value printed in the cell.

deviations should be higher for a larger footprint since it samples over a wider spatial region.

However, the ratios of $\sigma^2 T_b$ between the two satellites are not a straightforward function of resolution (Fig. 12). Rather, the comparison for some channels is dominated by higher noise in *N16* that is reflected in higher standard deviations. The largest differences are in the 15.0-, 14.7-, 14.5-, and 6.5-µm channels. The *N16* T_b histograms for these channels (similar to Fig. 7, not shown) form wide bell curves and are less distinct than those from *M1* upon inspection. Other channels do not show an obviously higher $\sigma^2 T_b$ from either satellite. Cirrus, overshooting, overlapping, and all types show an increase in $\sigma^2 T_b$ for most channels, but these $\sigma^2 T_b$ ratios are not substantially larger than those between HIRS/4 instruments depicted in Fig. 11.

In summary, we cannot distinguish instrument version differences between HIRS/3 and HIRS/4 from the intersatellite differences described previously, and from instrument degradation experienced by *N16*.

d. Diurnal variability

Here we briefly revisit the characterization of the diurnal cycle. Jackson and Soden (2007) develop a model of the diurnal cycle from HIRS data simulated in a GCM, in order to quantify the component of intersatellite "biases" due to the diurnal cycle. Lindfors et al. (2011) create a diurnal cycle by fitting a Fourier series to about 5 years of HIRS data, while MacKenzie et al. (2012) compare observed and modeled HIRS diurnal cycles. These studies focus on HIRS mid-IR channels and generally agree that clear-sky T_b peak around 1400–1600 LST over land. The

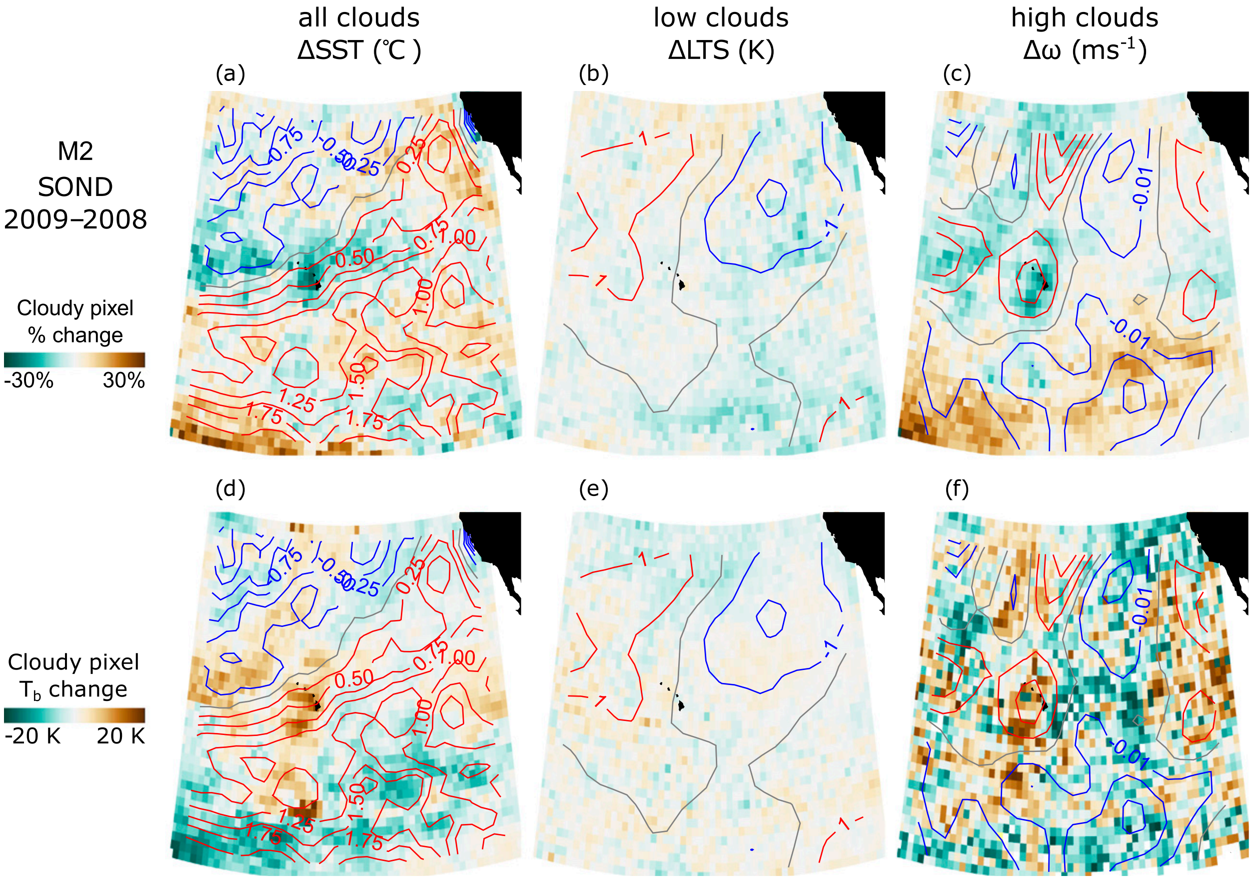

FIG. 14. (top row) *M2* cloudy footprint percentage changes (shading) and (bottom row) ΔT_b (shading) from SOND 2008 to 2009 for (a),(d) all clouds; (b),(e) low clouds; and (c),(f) high clouds. Colored contours (positive in red, zero in gray, and negative in blue) show changes from 2008 to 2009 in (a),(d) SSTs; (b),(e) LTS; and (c),(f) pressure velocity. LTS calculated as in Klein and Hartmann (1993) as the potential temperature difference between 700 and1000 hPa.

diurnal cycle amplitudes can be as high as 8 K, while over the ocean, they are generally <1 K. MacKenzie et al. (2012) posit that HIRS data are already sufficient to constrain the diurnal cycle over land and over sea, at least in the zonal mean. More specifically, while differences in the spectral response functions between satellites (in absence of recalibration) preclude the detection of trends, the diurnal variability may indeed be large enough to be characterized in spite of instrument differences. Note, however, that these studies also emphasize the smallness of the magnitude of the diurnal cycle over the ocean.

To test whether a cloud type–specific diurnal signal can be observed over the selected oceanic region, the *M2* data from 0930 LST is compared to *N19* data sampled around 1330 LST (not shown). Similar channel- and cloud type–specific mean T_b differences appear for this comparison of satellites as for those with overlapping ECTs; a few other pairs chosen to isolate components of the diurnal signal suggest very similar results. While some T_b differences could be explained by the diurnal variability of particular cloud types, the differences are smaller in magnitude than other contributing factors to intersatellite differences and variability. These results apply only to the oceanic region of study.

In summary, the diurnal cycle of mean T_b between 0930 and 1330 LST over the northeast Pacific Ocean region is generally <±1 K, with many cloud types slightly cooler during the morning orbit.

e. Interannual variability

To examine interannual variability, the T_b statistics are compared between 2008 and 2009 for *N18* during MAM and *M2* during SOND (Fig. 13). A transition from a La Niña to an El Niño occurred (Fig. 2) and both *N18* and *M2* experienced little change in the equatorial crossing time during this interval, making this an ideal opportunity for testing interannual differences. Although the results for both satellites and both seasons were investigated, the choice of satellite or season makes little difference to the results.

Therefore, we present here only results for *M2* during SOND.

The values of ΔT_b between 2008 and 2009 are small for SOND (Fig. 13a) in spite of the La Niña–to–El Niño transition (Fig. 2b). There appears to be a reduction in the T_b of the higher peaking CO_2-slicing channel during SOND, and a warming of T_b during MAM (not shown), although these anomalies are well within the range of previously described ΔT_b in section 5.

To physically diagnose the warming and cooling pattern seen in Fig. 13, we relate the geographical structure of cloud type percentages and cloud type–specific T_b to their dynamical and thermodynamical environment as depicted in the NNR (Fig. 14). SSTs warm in 2009 relative to 2008 in the tropical eastern Pacific and cool in the subtropics, sharpening the temperature gradient (Figs. 14a,d). Along with these increased SSTs is a decrease in lower-tropospheric stability (LTS) near the coast (Figs. 14b,e) and an increase in ascent (Figs. 14c,f). The decrease in LTS coincides with a decrease in the fraction of HIRS pixels identified as low-level clouds [cloud-top pressure (CTP) > 680 hPa]. The increase in ascent coincides with an increase in the fraction of HIRS pixels identified as high clouds (CTP < 400 hPa).

Satoh et al. (2012) find that warming sea surface temperatures favor increased cirrus cover, and narrower, more intense convective columns. During the warm phase in SOND 2009, there are lower T_b (Fig. 13) for most cloud types in the 14.5–15.0-μm bands, and lower T_b for opaque ice clouds across all channels indicates colder cloud tops that are associated with an increase in convective height and intensity.

In contrast to the regionally averaged ΔT_b between 2008 and 2009, the increasing $\sigma^2 T_b$ ratios between the two years (Fig. 13b) are striking. Increases in $\sigma^2 T_b$ for all pixels during MAM of the two years (not shown) are similar to those in SOND. For most cloud types, $\sigma^2 T_b$ are several tenths of a kelvin higher during 2009 than during 2008. The strongest increases in standard deviation occur for overshooting, cirrus, and opaque ice—all cloud types associated with deep tropical convection. Importantly, the modest percentage increase in $\sigma^2 T_b$ for *all* clouds belies the larger increases in variability for many cloud types, which are noticeable only when examining cloud type–specific statistics. These cloud type–specific statistics thus provide additional insight into physical processes. Specifically, we suggest that the increased variances are related to warmer SSTs, a strengthened overturning circulation, and a narrowing of convective cores during El Niño, as we describe below. Furthermore, the cloud type–specific $\sigma^2 T_b$ increases are much stronger than those due to intersatellite biases in Fig. 11b or year-to-year instrument degradation (a degradation of 10% per year for *M2* would be catastrophic indeed). *The general increase in* $\sigma^2 T_b$, with the emphasis on cloud types associated with the ITCZ, constitutes an example of region-specific interannual change that is likely detectable with the current state of calibration with the HIRS–AVHRR record.

The increase in $\sigma^2 T_b$ for all pixels during SOND includes a large contribution from changes in the tropical deep convective clouds (Fig. 13b). These changes can be explained by an increase in the convective cloud amount (Fig. 14c), an increase in height (and reduction in T_b, Fig. 14f), and possibly higher spatial variability in the warm phase [e.g., due to a narrowing and intensification of deep convection, as in Satoh et al. (2012)].

The higher spatial variability of convective clouds is likely related to the colder cloud tops in Figs. 13a, 14a,d. Specifically, an increase in the intensity of deep convection over the eastern Pacific warm pool should result in such colder cloud tops. Decreasing cloud-top temperature for deep convective clouds increases not only the range of cloud-top temperatures for the high clouds themselves, but also the variance due to any averaging of nearby, much warmer pixels.

Channel-by-channel changes also suggest an increase in deep convection and its impacts. The increase in $\sigma^2 T_b$ at the 14.5-μm channel, which peaks in the upper troposphere, and for the water vapor channels, suggests either 1) additional localized input of heat and moisture at these altitudes by deep convection or 2) contamination due to thin cirrus not detected by AVHRR. The smaller $\sigma^2 T_b$ ratios for channels that sense the mid- and lower troposphere hint at the latter.

Su and Jiang (2013) suggest that observed changes in high clouds during the 2009 El Niño are related to a strengthened tropical Hadley circulation. The observed increases in ascent, the decreases in LTS, and the overall shift from low to high clouds highlighted in Figs. 14b,c,f support their results.

In summary, a careful examination of both mean T_b and $\sigma^2 T_b$ by channel and cloud type helps to more clearly delineate cloud frequency, CTP, and opacity changes during a moderate shift toward the warm phase of El Niño. Analyzing changing HIRS T_b statistics by cloud type reveals cloud type–specific physical processes missed in the statistics for all pixels, and it confirms the results of earlier observational and modeling studies. Analyzing changing statistics by HIRS channel further highlights the upper-tropospheric impacts of deep convection. These variance changes are well outside the range of intersatellite differences aside from severe degradation.

6. Conclusions

We seek to produce a seamless, global-scale, long-term, continuous record of both cloud type and spectral T_b statistics, with the intent to better characterize clouds from seasonal to decadal time scales. Toward this end, we derive a cloud-typed spectral radiance record from NOAA polar-orbiting weather satellite data. Cloud properties are obtained from spectral imager data observed with the Advanced Very High Resolution Radiometer (AVHRR), where the cloud classification methods are defined by Clouds from AVHRR Extended (CLAVR-x) and the International Satellite Cloud Climatology Project (ISCCP) cloud-top pressure–optical thickness binning. Spectral brightness temperatures (T_b) observed by the High Resolution Infrared Radiation Sounder (HIRS) are characterized by the two aforementioned cloud type methodologies.

The above-mentioned characterization considers carefully the interpolation of AVHRR data onto each individual HIRS field of view (FOV). A conical point spread function (PSF) with a radius of approximately 8 km for HIRS/4 and 16 km for HIRS/3 is determined to be the most optimal PSF to interpolate AVHRR data to an individual HIRS FOV. The HIRS T_b are then characterized at the subpixel level and aggregates of cloud type statistics for large sets of T_b data are investigated. The T_b histograms sorted by cloud type are realistic for all HIRS channels; however, less overlap between adjacent cloud type histograms is observed with CLAVR-x cloud classification compared to ISCCP.

A novel method for mapping multiple statistical moments of large volumes of cloud-typed T_b data onto latitude and longitude grids using a memory-conserving, histogram-based approach is described. This approach is tested within the northeast tropical and subtropical Pacific Ocean. We compare and evaluate HIRS/AVHRR data in 2008 and 2009 among different satellite combinations during a significant ENSO transition to test whether changes in the cloud type spectral T_b observations can be quantified. The magnitude of T_b biases among spatially coincident satellite intersections over the northeast Pacific is a function of cloud type and wavelength. While the sign of the bias can change, the magnitudes are generally small for *NOAA-18* and *NOAA-19*, and *NOAA-19* and *MetOp-A* intersections. We further show that cloud-typed T_b variance changes well exceed intersatellite calibration uncertainties.

We argue that such higher-order statistical moments determined from spectral IR observations may serve as a useful long-term measure of changes in particular cloud types over the HIRS–AVHRR observing record. For example, we discern strong cloud type–dependent increases in T_b variance from 2008 (cool phase) to 2009 (warm phase), which are consistent with a strengthened overturning circulation, and an increase in deep convection during El Niño. These physical process changes are highly relevant to the study of climate variability and change.

The northeast Pacific Ocean case study also illustrates the need for further work on intercalibration between the various HIRS and AVHRR instruments. This intercalibration is shown to be a prerequisite for the determination of small shifts in the phase and magnitude of the diurnal cycle within each cloud type category over the ocean. Furthermore, we are unable to discern the effects of fundamental differences in the instrument resolution of HIRS from the effects of instrument degradation.

Acknowledgments. Portions of the research described in this paper were carried out at the Jet Propulsion Laboratory (JPL), California Institute of Technology, under a contract with the National Aeronautics and Space Administration. P. W. Staten, B. H. Kahn, and M. M. Schreier were supported by the NASA Satellite Calibration Interconsistency Studies program under Grant NNN13D968T directed by Lucia Tsaoussi. The HIRS and AVHRR level 1b data were processed and obtained from the NOAA Comprehensive Large Array-Data Stewardship System (http://www.class.ngdc.noaa.gov). NCEP reanalysis data are provided by the NOAA/OAR/ESRL/PSD, Boulder, Colorado (http://www.esrl.noaa.gov/psd/). The authors thank Hai-Tien Lee and Paul Menzel for their expertise and helpful discussions, as well as three anonymous reviewers for their helpful comments. Government sponsorship is acknowledged.

REFERENCES

Anderson, J., J. Dykema, R. Goody, H. Hu, and D. Kirk-Davidoff, 2004: Absolute, spectrally-resolved, thermal radiance: A benchmark for climate monitoring from space. *J. Quant. Spectrosc. Radiat. Transfer*, **85**, 367–383, doi:10.1016/S0022-4073(03)00232-2.

Baum, B. A., B. A. Wielicki, P. Minnis, and L. Parker, 1992: Cloud-property retrieval using merged HIRS and AVHRR data. *J. Appl. Meteor.*, **31**, 351–369, doi:10.1175/1520-0450(1992)031<0351:CPRUMH>2.0.CO;2.

——, R. F. Arduini, B. A. Wielicki, P. Minnis, and S.-C. Tsay, 1994: Multilevel cloud retrieval using multispectral HIRS and AVHRR data: Nighttime oceanic analysis. *J. Geophys. Res.*, **99**, 5499–5514, doi:10.1029/93JD02856.

Bender, F. A.-M., V. Ramanathan, and G. Tselioudis, 2011: Changes in extratropical storm track cloudiness 1983–2008:

Observational support for a poleward shift. *Climate Dyn.*, **38**, 2037–2053, doi:10.1007/s00382-011-1065-6.

Cao, C., K. Jarva, and P. Ciren, 2007: An improved algorithm for the operational calibration of the high-resolution infrared radiation sounder. *J. Atmos. Oceanic Technol.*, **24**, 169–181, doi:10.1175/JTECH2037.1.

Chen, R., C. Cao, and W. P. Menzel, 2013: Intersatellite calibration of NOAA HIRS CO_2 channels for climate studies. *J. Geophys. Res. Atmos.*, **118**, 5190–5203, doi:10.1002/jgrd.50447.

Choi, M., and B. Sweetman, 2010: Efficient calculation of statistical moments for structural health monitoring. *Struct. Health Monit.*, **9**, 13–24, doi:10.1177/1475921709341014.

Foster, M. J., and A. Heidinger, 2013: PATMOS-x: Results from a diurnally corrected 30-yr satellite cloud climatology. *J. Climate*, **26**, 414–425, doi:10.1175/JCLI-D-11-00666.1.

Frey, R. A., S. A. Ackerman, and B. J. Soden, 1996: Climate parameters from satellite spectral measurements. Part 1: Collocated AVHRR and HIRS/2 observations of spectral greenhouse parameter. *J. Climate*, **9**, 327–344, doi:10.1175/1520-0442(1996)009<0327:CPFSSM>2.0.CO;2.

Green, D. A., 2011: A colour scheme for the display of astronomical intensity images. *Bull. Astron. Soc. India*, **39**, 289–295.

Heidinger, A. K., and M. J. Pavolonis, 2009: Gazing at cirrus clouds for 25 years through a split window. Part I: Methodology. *J. Appl. Meteor. Climatol.*, **48**, 1100–1116, doi:10.1175/2008JAMC1882.1.

——, V. R. Anne, and C. Dean, 2002: Using MODIS to estimate cloud contamination of the AVHRR data record. *J. Atmos. Oceanic Technol.*, **19**, 586–601, doi:10.1175/1520-0426(2002)019<0586:UMTECC>2.0.CO;2.

——, R. Frey, and M. Pavolonis, 2004: Relative merits of the 1.6 and 3.75 μm channels of the AVHRR/3 for cloud detection. *Can. J. Remote Sens.*, **30**, 182–194, doi:10.5589/m03-058.

——, A. T. Evan, M. J. Foster, and A. Walther, 2012: A naive Bayesian cloud-detection scheme derived from *CALIPSO* and applied within PATMOS-x. *J. Appl. Meteor. Climatol.*, **51**, 1129–1144, doi:10.1175/JAMC-D-11-02.1.

——, M. J. Foster, A. Walther, and X. T. Zhao, 2014: The Pathfinder Atmospheres–Extended AVHRR climate dataset. *Bull. Amer. Meteor. Soc.*, **95**, 909–922, doi:10.1175/BAMS-D-12-00246.1.

Jackson, D. L., and B. J. Soden, 2007: Detection and correction of diurnal sampling bias in HIRS/2 brightness temperatures. *J. Atmos. Oceanic Technol.*, **24**, 1425–1438, doi:10.1175/JTECH2062.1.

Jin, H., and S. L. Nasiri, 2014: Evaluation of AIRS cloud-thermodynamic-phase determination with *CALIPSO*. *J. Appl. Meteor. Climatol.*, **53**, 1012–1027, doi:10.1175/JAMC-D-13-0137.1.

Joiner, J., H.-T. Lee, L. L. Strow, P. K. Bhartia, S. Hannon, A. J. Miller, and L. Rokke, 1998: Radiative transfer in the 9.6 μm HIRS ozone channel using collocated SBUV-determined ozone abundances. *J. Geophys. Res.*, **103**, 19 213–19 229, doi:10.1029/98JD01382.

Kahn, B. H., and J. Teixeira, 2009: A global climatology of temperature and water vapor variance scaling from the Atmospheric Infrared Sounder. *J. Climate*, **22**, 5558–5576, doi:10.1175/2009JCLI2934.1.

——, and Coauthors, 2014: The Atmospheric Infrared Sounder version 6 cloud products. *Atmos. Chem. Phys.*, **14**, 399–426, doi:10.5194/acp-14-399-2014.

Kalnay, E., and Coauthors, 1996: The NCEP/NCAR 40-Year Reanalysis Project. *Bull. Amer. Meteor. Soc.*, **77**, 437–471, doi:10.1175/1520-0477(1996)077<0437:TNYRP>2.0.CO;2.

Karlsson, J., G. Svensson, S. Cardoso, J. Teixeira, and S. Paradise, 2010: Subtropical cloud-regime transitions: Boundary layer depth and cloud-top height evolution in models and observations. *J. Appl. Meteor. Climatol.*, **49**, 1845–1858, doi:10.1175/2010JAMC2338.1.

Klein, S. A., and D. L. Hartmann, 1993: The seasonal cycle of low stratiform clouds. *J. Climate*, **6**, 1587–1606, doi:10.1175/1520-0442(1993)006<1587:TSCOLS>2.0.CO;2.

Li, J., W. W. Wolf, W. P. Menzel, W. Zhang, H.-L. Huang, and T. H. Achtor, 2000: Global soundings of the atmosphere from ATOVS measurements: The algorithm and validation. *J. Appl. Meteor.*, **39**, 1248–1268, doi:10.1175/1520-0450(2000)039<1248:GSOTAF>2.0.CO;2.

Lindfors, A. V., I. A. Mackenzie, S. F. B. Tett, and L. Shi, 2011: Climatological diurnal cycles in clear-sky brightness temperatures from the High-Resolution Infrared Radiation Sounder (HIRS). *J. Atmos. Oceanic Technol.*, **28**, 1199–1205, doi:10.1175/JTECH-D-11-00093.1.

MacKenzie, I. A., S. F. B. Tett, and A. V. Lindfors, 2012: Climate model–simulated diurnal cycles in HIRS clear-sky brightness temperatures. *J. Climate*, **25**, 5845–5863, doi:10.1175/JCLI-D-11-00552.1.

Marchand, R., 2013: Trends in ISCCP, MISR, and MODIS cloud-top-height and optical-depth histograms. *J. Geophys. Res. Atmos.*, **118**, 1941–1949, doi:10.1002/jgrd.50207.

Nasiri, S. L., and B. H. Kahn, 2008: Limitations of bispectral infrared cloud phase determination and potential for improvement. *J. Appl. Meteor. Climatol.*, **47**, 2895–2910, doi:10.1175/2008JAMC1879.1.

Norris, J. R., and A. T. Evan, 2015: Empirical removal of artifacts from the ISCCP and PATMOS-x satellite cloud records. *J. Atmos. Oceanic Technol.*, **32**, 691–702, doi:10.1175/JTECH-D-14-00058.1.

Pavolonis, M. J., and A. K. Heidinger, 2004: Daytime cloud overlap detection from AVHRR and VIIRS. *J. Appl. Meteor.*, **43**, 762–778, doi:10.1175/2099.1.

——, ——, and T. Uttal, 2005: Daytime global cloud typing from AVHRR and VIIRS: Algorithm description, validation, and comparisons. *J. Appl. Meteor.*, **44**, 804–826, doi:10.1175/JAM2236.1.

Robel, J., Ed., 2009: KLM user's guide with NOAA-N, -P supplement. [Available online at http://ncdc.noaa.gov/oa/pod-guide/ncdc/docs/klm/index.htm.]

Rossow, W. B., and R. A. Schiffer, 1991: ISCCP cloud data products. *Bull. Amer. Meteor. Soc.*, **72**, 2–20, doi:10.1175/1520-0477(1991)072<0002:ICDP>2.0.CO;2.

Satoh, M., S.-I. Iga, H. Tomita, Y. Tsushima, and A. T. Noda, 2012: Response of upper clouds in global warming experiments obtained using a global nonhydrostatic model with explicit cloud processes. *J. Climate*, **25**, 2178–2191, doi:10.1175/JCLI-D-11-00152.1.

Schreier, M. M., B. H. Kahn, A. Eldering, D. A. Elliott, E. Fishbein, F. W. Irion, and T. S. Pagano, 2010: Radiance comparisons of MODIS and AIRS using spatial response information. *J. Atmos. Oceanic Technol.*, **27**, 1331–1342, doi:10.1175/2010JTECHA1424.1.

——, ——, K. Sušelj, J. Karlsson, S. C. Ou, Q. Yue, and S. L. Nasiri, 2014: Atmospheric parameters in a subtropical cloud regime transition derived by AIRS and MODIS: Observed statistical variability compared to ERA-Interim. *Atmos. Chem. Phys.*, **14**, 3573–3587, doi:10.5194/acp-14-3573-2014.

Shi, L., and J. J. Bates, 2011: Three decades of intersatellite-calibrated High-Resolution Infrared Radiation Sounder upper tropospheric water vapor. *J. Geophys. Res.*, **116**, D04108, doi:10.1029/2010JD014847.

——, ——, and C. Cao, 2008: Scene radiance–dependent intersatellite biases of HIRS longwave channels. *J. Atmos. Oceanic Technol.*, **25**, 2219–2229, doi:10.1175/2008JTECHA1058.1.

Soden, B. J., D. L. Jackson, V. Ramaswamy, M. D. Schwarzkopf, and X. Huang, 2005: The radiative signature of upper tropospheric moistening. *Science*, **310**, 841–844, doi:10.1126/science.1115602.

Strabala, K. I., S. A. Ackerman, and W. P. Menzel, 1994: Cloud properties inferred from 8–12-μm data. *J. Appl. Meteor.*, **33**, 212–229, doi:10.1175/1520-0450(1994)033<0212:CPIFD>2.0.CO;2.

Su, H., and J. H. Jiang, 2013: Tropical clouds and circulation changes during the 2006/07 and 2009/10 El Niños. *J. Climate*, **26**, 399–413, doi:10.1175/JCLI-D-12-00152.1.

Sun, B., M. Free, H. L. Yoo, M. J. Foster, A. Heidinger, and K.-G. Karlsson, 2015: Variability and trends in U.S. cloud cover: ISCCP, PATMOS-x, and CLARA-A1 compared to homogeneity-adjusted weather observations. *J. Climate*, **28**, 4373–4389, doi:10.1175/JCLI-D-14-00805.1.

Teixeira, J., and Coauthors, 2011: Tropical and subtropical cloud transitions in weather and climate prediction models: The GCSS/WGNE Pacific Cross-Section Intercomparison (GPCI). *J. Climate*, **24**, 5223–5256, doi:10.1175/2011JCLI3672.1.

Thomas, S. M., A. K. Heidinger, and M. J. Pavolonis, 2004: Comparison of NOAA's operational AVHRR-derived cloud amount to other satellite-derived cloud climatologies. *J. Climate*, **17**, 4805–4822, doi:10.1175/JCLI-3242.1.

Turner, E., and S. Tett, 2014: Using longwave HIRS radiances to test climate models. *Climate Dyn.*, **43**, 1103–1127, doi:10.1007/s00382-013-1959-6.

Walther, A., and A. K. Heidinger, 2012: Implementation of the daytime cloud optical and microphysical properties algorithm (DCOMP) in PATMOS-x. *J. Appl. Meteor. Climatol.*, **51**, 1371–1390, doi:10.1175/JAMC-D-11-0108.1.